Journal of Controlled Release 386 (2025) 114151

Contents lists available at ScienceDirect

Journal of Controlled Release

journal homepage: www.elsevier.com/locate/jconrel

Microvascular and astrocytic responses to repeated magnetic resonance-guided focused ultrasound

Sébastien Rigollet [a,b,*], Aurélien Delphin [c], Lucie Chalet [d], Thomas Ador [e], Erik Dumont [b], Benjamin Lemasson [a], Thomas Christen [a], Chantal Pichon [e,f], Anthony Delalande [e], Vasile Stupar [a,c], Emmanuel L. Barbier [a,c]

[a] Univ. Grenoble Alpes, Inserm, U1216, Grenoble Institut des Neurosciences, 38000 Grenoble, France
[b] Image Guided Therapy, Pessac, France
[c] Univ. Grenoble Alpes, Inserm, US17, CNRS, UAR3552, CHUGA, IRMaGe, 38000 Grenoble, France
[d] Department of Neuroscience Imaging and Clinical Sciences (DNISC), Institute for Advanced Biomedical Technologies (ITAB), 'G. d'Annunzio University' of Chieti-Pescara, Chieti, Italy
[e] ART ARNm Inserm UMS 55 and LI2RSO-University of Orléans, Orléans F-45100, France
[f] Institut Universitaire de France, 1 rue Descartes, Paris F-75035, France

ARTICLE INFO

Keywords:
Focused ultrasound
Quantitative MRI
MR fingerprinting
Perfusion
Neuroinflammation

ABSTRACT

Focused ultrasound (FUS), in combination with microbubbles, enables the transient and localized opening of the blood–brain barrier (BBB) for targeted drug delivery. While this technique has shown promise in preclinical models, the safety and neurovascular consequences of repeated BBB permeabilization remain incompletely understood. In this study, we performed a longitudinal assessment of vascular, microstructural, and glial responses following repeated FUS-mediated BBB opening in healthy rats using magnetic resonance (MR)-guided targeting and MR vascular fingerprinting. FUS sessions were conducted on a weekly or twice-weekly basis over a period of four weeks, employing two distinct acoustic pressures, 390 kPa and 440 kPa, respectively. The BBB opening was reproducible across sessions, with stable contrast enhancement observed with DCE-MRI and a homogeneous cumulative open BBB volume. No significant hemorrhages or edema were detected; however, transient cerebral blood flow reductions of approximately 15–20 % were observed following each session. After eight FUS sessions at 440 kPa, subtle vascular remodeling was observed, including increased vessel radius and reduced tissue oxygen saturation. This finding was confirmed by both MRI and histological analysis. Astrocytic activation, as determined by GFAP immunostaining, was minimal after a single or weekly FUS exposure but became significant with biweekly treatments, indicating a cumulative neuroimmune response. These results support the feasibility of weekly FUS-induced BBB opening at moderate acoustic pressures. However, they also underscore the importance of protocol optimization to prevent glial and vascular stress in long-term therapeutic applications.

1. Introduction

The blood-brain barrier (BBB) regulates nutrient delivery and prevents harmful substances from entering the brain. It is a key component of the neurovascular unit (NVU), which tightly regulates cerebral blood flow (CBF) to ensure proper oxygen and nutrient supply to neurons [1]. However, BBB poses a major challenge for delivering therapeutic agents to the brain, making the treatment of neurological disorders particularly difficult. One promising non-invasive approach to overcome this barrier is the use of focused ultrasound (FUS) in combination with

Abbreviations: ADC, apparent diffusion coefficient; AUC, area under the curve; BBB, blood-brain barrier; CBF, cerebral blood flow; CE, contrast enhancement; DCE-MRI, Dynamic Contrast-Enhanced MRI; FUS, focused ultrasound; GFAP, glial fibrillary acidic protein; H&E, hematoxylin and eosin; MGE3D, Multi-Gradient Echo 3D; MGESFIDSE, Multi-Gradient Echo Sampling of FID and Spin-Echo; MI, mechanical index; MRgFUS, MR-guided FUS; MRI, magnetic resonance imaging; MSME, Multi-Slice Multi-Echo; MRvF, MR vascular Fingerprinting; NVU, neurovascular unit; pCASL, pseudo-continuous arterial spin labeling; PNP, peak negative pressure; QSM, Quantitative susceptibility mapping; R, averaged vessel radius; SD, standard deviation; SO_2, oxygen saturation; USPIO, ultra-small paramagnetic iron oxide; Vf, volume fraction.

* Corresponding author at: Univ. Grenoble Alpes, Inserm, U1216, Grenoble Institut des Neurosciences, 38000 Grenoble, France.
E-mail address: sebastien.rigollet@univ-grenoble-alpes.fr (S. Rigollet).

https://doi.org/10.1016/j.jconrel.2025.114151
Received 20 June 2025; Received in revised form 17 August 2025; Accepted 19 August 2025
Available online 20 August 2025

microbubbles, which can induce a transient and reversible BBB disruption, and thereby enhance drug delivery. Preclinical and clinical studies have demonstrated the potential of FUS-mediated BBB opening in various applications, including brain tumors and Alzheimer's disease [2–5].

In addition to BBB opening and in absence of observable tissue damage, FUS also induces a wide range of biological responses within the brain parenchyma and vasculature: alteration of tight junctions, vascular dilation or constriction [6–8], altered neurovascular coupling [9,10], transient blood flow reduction [6,11], and neuroinflammatory processes such as activation of astrocytes and microglia [6,12,13], increased cytokine expression (interleukin-1 beta, interleukin-6, chemokine ligands 2, 3 and 7) [14,15], and recruitment of immune cells [16–18]. While these effects are often transient (a few days) and reversible after a single exposure, they could become more pronounced or persistent in case of repeated BBB opening, a therapeutic approach regularly proposed for brain tumors and Alzheimer's disease at preclinical and clinical level (Table 1).

A number of studies have reported that repeated FUS-induced BBB opening does not result in significant adverse effects in various animal models, including wild-type mice [30], Alzheimer's disease mice models [24–27], rats and non-human primates [31–35], as well as in glioblastoma patients [3,21–23] and Alzheimer's patients [28,29]. Repeated BBB openings have the potential to amplify the tissue alterations previously mentioned or to trigger more complex domino effects, particularly when such openings occur before the tissue has fully recovered from the previous treatment. Furthermore, while some studies have examined behavioral and inflammatory outcomes following weekly treatments [30,32,33], the impact on the cerebral microvasculature remains largely unexplored, despite the significant CBF reduction following single BBB opening previously reported [6,11].

To investigate microvascular effects in vivo, magnetic resonance imaging (MRI) remains a non-invasive gold standard. MRI techniques can provide valuable quantitative information about perfusion, diffusion, and BBB integrity. In addition, emerging methods like MR vascular Fingerprinting (MRvF) offer a powerful new tool to capture, in a single acquisition, multiple microvascular parameters such as averaged microvascular radius (R), tissue oxygen saturation (SO_2), and blood volume (Vf) [36–38]. This emerging approach has shown promise in detecting subtle microvascular changes in preclinical models of brain tumors [38].

In this study, we assessed the microvascular and glial response to repeated FUS-mediated BBB opening in healthy rat brains. Weekly and bi-weekly FUS-induced BBB permeabilization were performed for 4 weeks, using a preclinical relevant protocol based on moderate acoustic pressures, suitable for evaluating therapeutic delivery strategies. Animals were monitored over time using in vivo MRI, including MRvF, to map signs of edema and hemorrhage, CBF, Vf, R, SO_2 and FUS-induced BBB permeability to gadolininum-chelate. One week after the last FUS session, a histological analysis was performed to evaluate astrocytic and endothelial markers. Observations in these two groups were compared to the contralateral healthy tissue, which underwent repeated anesthesia but not BBB opening. Additionally, a control group underwent a single FUS-mediated BBB opening.

Table 1
Examples of repeated FUS treatment studies for brain tumors and Alzheimer's disease-related studies. In gray are highlighted the clinical studies with ($) implantable US device (SonoCloud-1 or 9, Carthera, Lyon, France) or (£) external MRgFUS device (ExAblate Neuro, Insightec, Tirat Carmel, Israël).

	Model and disease	Delay between two FUS sessions	Number of FUS sessions	Study
Brain tumor	9 L Fischer rat	1 week	3	[19]
	F98 Fischer rat	3 weeks	2	[20]
	Glioblastoma patient	1 month	6	[3,21] $,£
	Glioblastoma patient	3 weeks	Up to 6	[22] $
	Glioblastoma patient	1 month	10	[23] $
Alzheimer's disease	K369I tau mice	1 week	15	[24]
	3 × Tg-AD mice	1 week	6	[25]
	APP23 mice	2 weeks	4	[26]
	rTg4510 mice	1 week	4	[27]
	Alzheimer's patient	3 weeks	6	[28] $
	Alzheimer's patient	2 weeks	3	[29] £

2. Materials and methods

2.1. Animal care and groups

Every animal experiment was conducted under the ethical guidelines of both the local Ethics committee (GIN 04CE) and the French Ministry of Research and Health (Authorization APAFIS #43777). Forty-three Wistar Han rats from Janvier Labs (Le Genest-Saint-Isle, France) were randomized in 3 groups. The first two groups are the core of this study: the 4-FUS group received 4-FUS sessions over 4 weeks ($n = 13$) and the 8-FUS group received 8-FUS sessions over 4 weeks ($n = 14$). The single-FUS group corresponds to animals that received one FUS application, for control purposes, and evaluated at 4 different time points after FUS ($n =$ 4 animals per time point leading a total of 16 animals in that group). In all groups, two levels of ultrasonic peak negative pressure (PNP) were used: 390 and 440 kPa. For sake of comparison with previous studies, we also report here the corresponding mechanical indexes (MI): 0.32 and 0.36, respectively although MI only applies to short diagnostic pulses, strictly speaking. These settings previously demonstrated efficient drug delivery in the context of various brain diseases including Huntington's disease and glioblastoma [39,40].

All animals underwent one or several sessions in which MR-guided FUS (MRgFUS; see below for details) was performed, followed by an MRI exam (short or long MRI protocol, see below for details). Eventually, the animal was euthanized and histology was performed. For all in vivo procedures, animals were anesthetized with a mixture of air and oxygen (80/20 %) and isoflurane (4 % for induction; 1.5–2 % for maintenance). When needed, a 24G catheter was inserted in the tail vein for intravenous injections of saline, gas microbubbles and contrast agents. At the end of each experimental procedure, animals were placed in a cage under a heating lamp until they regained full consciousness (Fig. 1.A). The details of the protocol for each group are (Fig. 1.B):

- For the single-FUS group, the short MRI protocol was performed. Some animals were euthanized either 3 h or 1 day after MRgFUS. In addition, some animals underwent the long MRI protocol either 1 week or 4 weeks after MRgFUS and were euthanized at the end of the MRI session;
- For the 4-FUS group, the MRgFUS and the long MRI protocol were performed once a week. Animals were euthanized one week after the last MRgFUS/MRI session, i.e. 5 weeks after the first FUS session;
- For the 8-FUS group, the MRgFUS, performed twice a week (i.e., once every three to four days) and followed by either the short or the long MRI protocol, in an alternating manner to limit the effects of anesthesia and cumulative agent doses [41]. Thereby, the MRI protocol was used for sessions 1, 3, 5, and 7 and the long MRI protocol for sessions 2, 4, 6, and 8. Animals were euthanized one week after the last MRgFUS/MRI session, i.e. 5 weeks after the first FUS session.

The weight and the general behavior of animals were monitored throughout the entire study with a scoring grid, including assessments of food intake, posture, and facial expression. The characteristics of each group and the initial animal weight are displayed in Table 2. The details

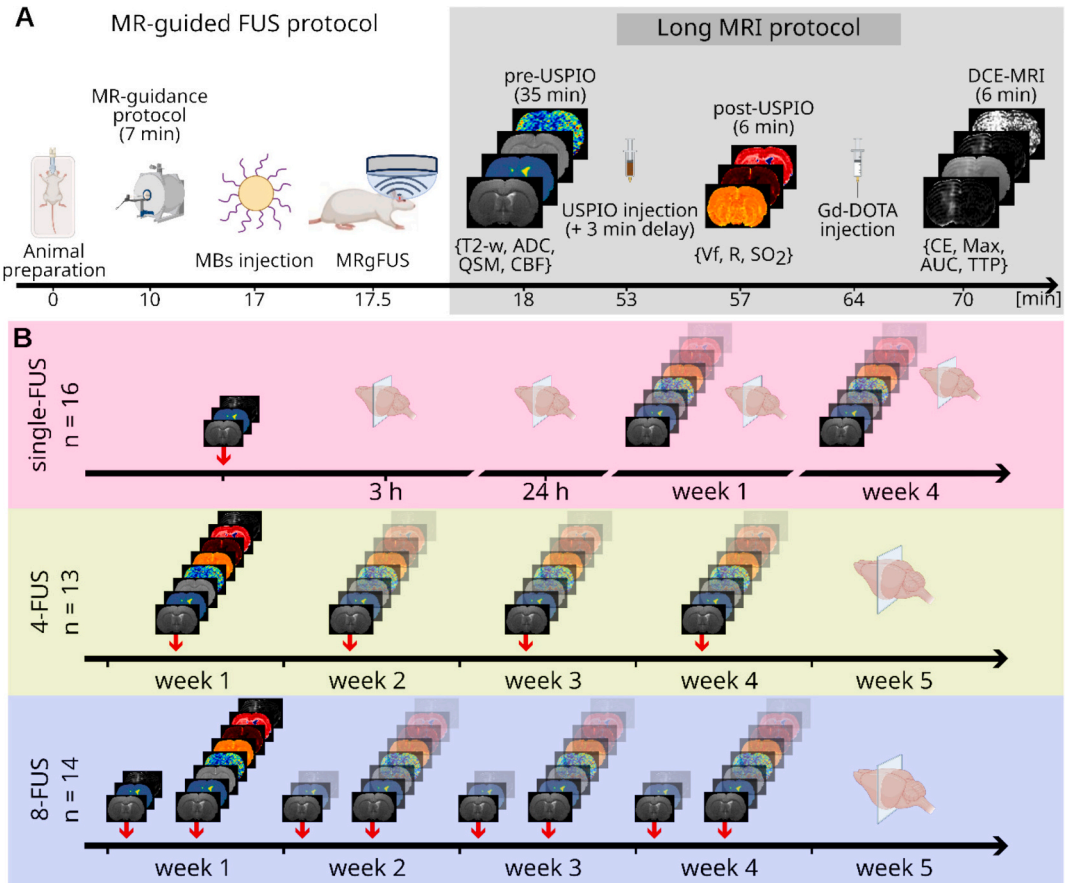

Fig. 1. Overview of the experimental timeline. A) Schematic representation of a single FUS session protocol, including animal preparation, MR-guidance, intravenous injection of microbubbles, FUS application, and long MRI protocol. B) Experimental timeline for single-FUS, 4-FUS, and 8-FUS groups. Single-FUS animals ($n = 16$) were assessed at multiple timepoints (1 h, 3 h, 24 h, 1 week, and 4 weeks post-treatment) with MRI and histology. Repeated FUS groups (4- and 8-FUS; $n = 13$ and 14 per group) underwent FUS and MRI once or twice per week. Animals were euthanized at week 5.

Table 2
Number of animals per group with the different histological analysis timepoints and average weight at the beginning of the procedure (mean ± SD).

Group	in situ PNP	Histology time point	number of animals	Weight [g]
Single-FUS	440 kPa	3 h post-FUS	4	387 ± 17
	440 kPa	24 h post-FUS	4	405 ± 13
	440 kPa	1-week post-FUS	4	227 ± 13
	440 kPa	4 weeks post-FUS	4	328 ± 5
4-FUS	390 kPa	1-week post-FUS	6	286 ± 49
	440 kPa	1-week post-FUS	7	299 ± 30
8-FUS	390 kPa	1-week post-FUS	7	318 ± 14
	440 kPa	1-week post-FUS	7	273 ± 22
		Total	43	

of the MRgFUS, MRI, and histology protocols are given below.

2.2. MR-guided FUS

BBB opening was performed using an MRgFUS system (Image Guided Therapy, Pessac, France) previously described and characterized [6,42]. Briefly, this setup incorporates a transducer with seven concentric elements (Imasonic, Voray-sur-l'Ognon, France) which allows control of the US focal length by steering (center frequency: 1.5 MHz, radius of curvature: 20.01 mm, F = 0.8). The transducer was calibrated using a bullet hydrophone (HGL-0200, ±3-dB frequency range of 0.25–40 MHz; Onda Corporation, Sunnyvale, CA, USA) [6]. The animals were positioned in the MRgFUS cradle, after the hair on their scalp was removed with an electric razor and depilatory cream. Their heads were fixed with a tooth bar and a nose cone that delivered the anesthetic mixture. Echographic gel was applied on the scalp to ensure optimal acoustic coupling with the transducer membrane. The MRgFUS system was positioned at the center of the 4.7 T MRI scanner (see below). Two series of images (axial and coronal T_1-weighted RARE) were acquired to localize the FUS transducer. Then, using a third image series (T_2-weighted TurboRARE), a FUS trajectory (raster scan of a 3.2 × 4 mm^2 area) was delineated to permeabilize a region encompassing the striatum (Fig. 3.E). Prior to the FUS application, 1.5×10^8 homemade lipidic microbubbles diluted in a volume of 100 µL of HEPES buffer (10 mM, 7.4 pH) were injected intravenously as a bolus through the tail vein and flushed with 50 µL of NaCl. To better characterize the administered dose, we calculated the Microbubble Volume Dose (MVD) [43]. The resulting MVD was ~3 µL/kg. Briefly, microbubbles were composed of 1,2-distearoyl-sn-glycero-3-phosphocholine (Merck, Darmstadt, Germany) and 1,2-dimyristoyl-sn-glycero-3-phospho-ethanolamine-N-[methoxy (polyethyleneglycol)-2000] (Merck, Darmstadt, Germany) (88:12 M ratio) and prepared by thin film hydration method as detailed previously [6,44]. Microbubbles initially lyophilized were filled with perfluorobutane gas (F2 Chemicals, Preston, UK), rehydrated with 500 µL of HEPES buffer and activated by mechanical agitation with a VIALMIX (Bristol-Myers Squibb, Princeton, NJ, USA) during 45 s. Following their activation, microbubbles had a mean diameter of 1.4 ± 0.9 µm and a concentration of $2.35 \times 10^{10} \pm 1.93 \times 10^9$ MBs/mL. Continuous FUS pulses were delivered along the whole previously defined trajectory with a 50-ms pause at each direction change to avoid accumulation of acoustic energy, as previously reported [39,45]. The FUS application

(raster scan) was repeated 10 times for a total duration of 34 s. At the end of the FUS procedure, the MRgFUS system was removed from the MRI scanner prior to performing an MRI protocol.

2.3. MRI acquisition and analysis

2.3.1. MRI acquisition

MRI was performed using a 4.7 T scanner (Avance III, Bruker, Ettlingen, Germany) equipped with a volume transmit coil and a single-element surface receive coil (Bruker, Ettlingen, Germany) at the IRMaGe small animal imaging facility (Grenoble, France) and operating under ParaVision 6.0.1. Two different MRI protocols were performed (Sequence parameters are detailed in Table 3):

- The long MRI protocol (55 min duration) assessed anatomy, microstructural integrity, CBF and other vascular properties (R, Vf, SO_2), and BBB permeability as follows (Fig. 1.A).

An anatomical reference image was obtained using a T_2-weighted TurboRARE sequence. Then, the apparent diffusion coefficient (ADC) of water was assessed via Diffusion Tensor Imaging using Echo-Planar Imaging (DTI-EPI) and CBF using a pseudo-continuous arterial spin labeling (pCASL) approach, including a map of tissue T_1 and a measure of the labeling inversion efficiency, as previously described [46]. Quantitative susceptibility mapping (QSM) data were calculated from a Multi-Gradient Echo 3D (MGE3D) sequence to assess potential accumulation in tissue of ultra-small paramagnetic iron oxide (USPIO) nanoparticles. A Multi-Slice Multi-Echo (MSME) sequence was used for T_2 mapping. In order to derive R, Vf and SO_2, two MGESFIDSE (Multi-Gradient Echo Sampling of FID and Spin-Echo) acquisitions were performed before and 3 min after intravenous injection USPIO nanoparticles (200 μmol of iron / kg, Synomag-D 50 nm, Micromod, Rostock, Germany) [36,47,48]. Finally, BBB permeability was quantified using a Dynamic Contrast-Enhanced MRI (DCE-MRI) protocol with an intravenous injection of Gd-DOTA (200 μmol/kg, Dotarem®, Guerbet, Villepinte, France).

- The short MRI protocol (13 min duration) only included anatomy T_2-weighted, microstructural integrity (DTI-EPI) and BBB permeability (DCE-MRI).

2.3.2. MRI processing

ADC maps were calculated using ParaVision 6.0.1. (Fig. 2.B). All other quantitative images, except the QSM map, were processed with modules implemented in MP3 software [49]. CBF maps (Fig. 2.D) were derived from the pCASL dataset using the methodology described by Hirschler et al. [46].

QSM maps (Fig. 2.C) were computed as described by Chalet et al. and based on the phase signal of the mGRE acquisition. Complex non-linear fitting followed by Laplacian operation provided temporal and spatial phase unwrapping, respectively [50,51]. Background field extraction was performed with V-SHARP as recommended by the QSM Consensus Organization Committee [52] and total magnetic susceptibility maps were reconstructed with star-QSM [53]. The χ-separation implementation was used to separate diamagnetic (χ+) and paramagnetic (χ-) susceptibility sources [54]. R_2' relaxation rate was obtained with R_2*-based auto-regression on linear operations fitting and a nominal R_2 value of 13 Hz [55].

R, Vf, and SO_2 maps were obtained using the MR vascular fingerprint approach (MRvF) [37]:

- A dictionary of 28,000 MRI signals was simulated based on as many MRI-sized voxels of 248 × 248 × 744 μm^3. Each MRI-voxel included a microvascular network derived from a brain microscopy dataset in healthy mice [36] and was associated with a 4-dimension parameter space (T_2, R, Vf and SO_2). The water diffusion coefficient was set to 1000 $\mu m^2/s$. MR simulations were performed using in-house Matlab software (The MathWorks Inc., Natick, MA, USA), considering a main magnetic field of 4.7 T [56];
- Acquired MR signals with the MGESFIDSE sequence before and after the injection of USPIO were concatenated. Thereby, a fingerprint per voxel was obtained.
- A Bayesian-based learning approach [57] was used to learn the relationship between the dictionary-signals and the corresponding parameter space. Once trained, the algorithm receives a fingerprint and produces T_2, R, Vf and SO_2 values. Representative examples of R, Vf and SO_2 maps obtained with this approach are displayed in Fig. 2. *E*-G.

To evaluate BBB permeability, the area under the curve (AUC) and contrast enhancement (CE) were derived from the DCE-MRI (see Fig. S2). The open BBB area was delineated manually based on these images.

2.3.3. Atlas, data registration and ROI determination

The brains were masked using the PCNN3D algorithm in raw T_2-weighted images [58]. The masked T_2-weighted images of the following MRI sessions were all registered to the first MRI session using the FMRIB's Linear Image Registration Tool from FSL software, twelve-parameter affine registrations, and a trilinear interpolation [59]. The transformation thereby obtained was then applied to every scan acquired during the session and the delineated ROI. The SIGMA rat brain template and atlas were registered to each subject's imaging space for data analysis [60].

After image registration, the intersection of the open BBB across all treatment sessions was recovered to compute the average permeabilized volume. The open BBB area extended across several brain regions, including the striatum, the corpus callosum, the thalamus and the ventricles. We performed the analysis of our parameters in the striatum as this was the region mostly permeabilized. The term "ipsilateral region" hereafter refers to the striatum that was targeted four times for the 4-FUS group and eight times for the 8-FUS group.

Table 3
Main parameters of the MRI sequences used in this study. ΔTE: echo spacing; FOV: field of view; Inv. Eff.: Inversion efficiency of the pseudo-continuous arterial spin labeling; T1-MTI: T1-Multi-inversion times; LD: label duration; PLD: post labeling delay; TE: echo time; TIs: inversion times; TR: repetition time.

Sequence	TR/TE [ms]	FOV [mm^2]	matrix size	voxel size [μm^3]	Other parameters	T_{acq}
T_2 TurboRARE	2200/36	30 × 30	256 × 256	117 × 117 × 1000	RARE-factor = 8	3 min 31 s
DTI-EPI	2200/33	30 × 30	128 × 128	234 × 234 × 1000	b-values = 0, 800 $s.mm^{-2}$	3 min 31 s
Inv. Eff.	225/3.6	30 × 30	256 × 256	117 × 117 × 1000	1 mm-thick slice	3 min 30 s
T1-MTI	10,000/19	30 × 30	128 × 128	234 × 234 × 1000	18 TIs = {30; 10,000 ms}	4 min
pCASL	4000/21	30 × 30	128 × 128	234 × 234 × 1000	30 repetitions, LD = 3000 ms, PLD = 300 ms	4 min
MGE3D	TR = 100 ms; TE_1 = 4 ms	30 × 30	128 × 128	234 × 234 × 1000	ΔTE = 4.53 ms; 15 grad. Echoes	8 min 58 s
MSME	TR = 2350 ms; TE_1 = 12 ms	30 × 30	128 × 128	234 × 234 × 1000	ΔTE = 12 ms; 26 spin echoes	3 min 46 s
MGESFIDSE	TR = 4000 ms; TE_1 = 2.2 ms	30 × 30	128 × 128	234 × 234 × 1000	ΔTE = 2.3 ms; 32 echoes; spin echo time = 60 ms	6 min 24 s
DCE-MRI	800/4	30 × 30	128 × 128	234 × 234 × 1000	Gd-DOTA injection at 1 min	6 min 20 s

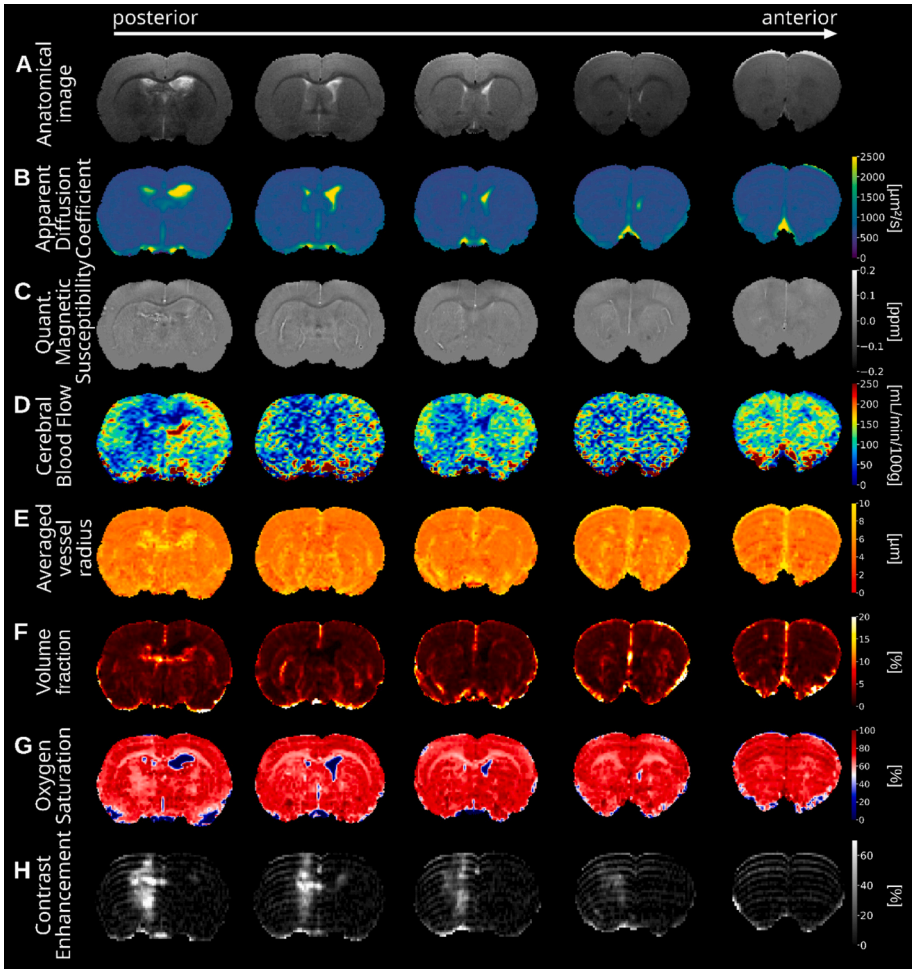

Fig. 2. Representative examples of the different parametric MRI maps obtained in this study. All images are from the last timepoint from a representative subject that received 8-FUS sessions at 440 kPa. Anatomical image (A), ADC (B), QSM (C), CBF (D), R (E), Vf (F), SO2 (G), and CE (H) maps. In the latter, the mild banding artifact arises from the method used to accelerate image acquisition.

2.4. Histology protocol

Brains were swiftly excised and immediately frozen in -80 °C isopentane, then stored at -80 °C. Cryosections (10 µm) spanning different levels along the anteroposterior axis were obtained using a cryotome set at -20 °C. To allow for multiple analyses, sections for different stainings, including hematoxylin and eosin (H&E) as well as immunohistochemical markers targeting the vascular system and neuroinflammatory processes, were interleaved.

For immunohistochemistry, sections were fixed in paraformaldehyde (Fluka Chemie AG, Buchs, Switzerland) and incubated overnight at 4 °C with primary antibodies: rabbit anti-glial fibrillary acidic protein (GFAP) (1:1000, DAKO, 70334) for astrocytes, and mouse anti-SMI 71 (1:1000, BioLegend, 836803) for BBB integrity. After primary antibody incubation, sections were treated with species-specific fluorophore-conjugated secondary antibodies: goat anti-rabbit (1:1000, Invitrogen, A11008) and donkey anti-mouse (1:1000, ThermoFisher, A31540). Sections were then counterstained with DAPI (ThermoFisher) for nuclei visualization, mounted with coverslips, and rinsed in PBS-Tween 0.1 %.

Images were digitized using the Axioscan scanner (Zeiss, Oberkochen, Germany) at the PIC-GIN photonic imaging platform (Grenoble, France) and analyzed using ZEN 3.6 (Zeiss) and Python 3.10.0.

For H&*E*-stained sections, a visual inspection of the entire slice was performed, with particular attention to the FUS-treated regions in order to detect any alteration or microhemorrhage.

For immunofluorescence GFAP staining analysis, the analysis was performed using a custom Python pipeline developed with the *OpenCV* library. Briefly, we binarized images and applied an Otsu threshold, removed the small (< 250 pixels) and large objects (> 2000 pixels) that could pollute the image and extracted three metrics to quantify astrocyte reactivity: astrocytic density, area occupation, and mean fluorescence intensity.

Three key morphometric parameters were extracted from the histological images of blood vessels: vessel length, mean radius, and tortuosity. The analysis was performed using a custom Python pipeline developed with the *OpenCV*, *NumPy*, *SciPy*, and *scikit-image* libraries [61–63]. Histological images were binarized using Otsu's thresholding method. To reduce noise and remove small artifacts, binary masks were filtered to exclude small objects (750 pixels), followed by a binary dilation (10 pixels) to fill small gaps in vessel structures. The contours of the remaining objects were extracted and skeletonized. The mean radius of each segmented vessel was computed by applying a distance transform on the binary mask to estimate the distance from the skeleton of the vessel to its edge. The local radius values along the skeleton were averaged to obtain the mean vessel radius. Vessel length was determined using the perimeter of each contour. Tortuosity was calculated as the ratio of the vessel's real length (number of points along the path) to Euclidean distance between its two endpoints.

2.5. Statistical analysis

Statistical analysis was conducted using Python 3.10.0, with the

Scipy libraries [62]. Pairwise comparisons were performed using the Wilcoxon signed-rank test, and comparisons between independent groups were conducted using the Mann–Whitney *U* test. The significance level (α) was set at 0.05, meaning that *p*-values below 0.05 were considered statistically significant. Data are presented as mean ± standard deviation (SD).

3. Results

3.1. Repeated BBB permeabilization is reproducible with MR-guided FUS device without compromising the BBB integrity

The BBB was successfully and reproducibly permeabilized in all animals using MRgFUS at either 390 or 440 kPa (Fig. 3.*E*-F). This protocol enabled targeted and repeated BBB opening in the same brain region across all FUS sessions in both the 4-FUS and 8-FUS groups (Fig. 3.A).

The open BBB volume for each FUS session is presented in Fig. 3.B, showing an average open BBB volume of 61 ± 25 mm^3 (see Fig. S1.A for the distribution of open BBB volumes). For each animal, we computed the repeated open BBB volume, i.e. the volume over which the BBB is repeatedly open at each session. Across the 27 animals from 4-FUS and 8-FUS groups, 25 showed repeated open BBB volume of 28 ± 11 mm^3 which represents about 46 % of the mean open BBB volume (Fig. 3.B-C). Two animals, with repeated open BBB volumes below 10 mm^3, were excluded from subsequent analyses.

In the 4-FUS groups, the repeated open BBB volumes were 29 ± 17 mm^3 at 390 kPa and 32 ± 16 mm^3 at 440 kPa. In the 8-FUS groups, repeated open BBB volumes were 23 ± 12 mm^3 and 29 ± 12 mm^3 at 390 and 440 kPa, respectively. No statistically significant differences were found between acoustic pressures or FUS-session regarding the repeated open BBB volume (Fig. 3.C), indicating the reproducibility of the procedure.

Regarding BBB permeability (Fig. 3.D-G), a consistent and significant increase in AUC was observed in the ipsilateral region following each FUS exposure. Notably, the CE in the ipsilateral region was at least 1.5-fold larger than that in the contralateral region across all sessions (see Fig. S1.B), with no significant temporal variations in either CE or AUC values. These results indicate that repeated BBB permeabilization yields consistent levels of permeability over time, suggesting that the BBB ability to reopen is not progressively altered by treatment.

3.2. Safety of the procedure

Across all groups, no signs of behavioral degradation or altered food intake were detected. All animals gained weight throughout the study (Fig. S3), with slightly faster weight gain observed in the single-FUS group compared to the 4-FUS and 8-FUS groups; however, the differences were not statistically significant. This trend could be ascribed to repeated anesthesia and/or repeated FUS.

Histological evaluation of H&*E*-stained brain sections revealed no lesions in the ipsilateral hemisphere at all timepoints following a single-FUS procedure. High-magnification images of the striatum and choroid plexus at 3 h post-treatment confirmed the absence of damage in the FUS-targeted regions (Fig. 4.A). In later timepoints, no micro-hemorrhages were observed at 24 h, 1 week, or 4 weeks post-single-FUS (Fig. 4.B). Small lesions were observed in the 4-FUS and 8-FUS groups one week after the last FUS session. A gradual increase in lesion count was found with higher acoustic pressure and repeated FUS sessions (1/4 animal lesion in 4-FUS groups, 4/7 in 8-FUS at 390 kPa and 5/7 in 8-FUS at 440 kPa) (Fig. 4.B). For instance, in the 8-FUS group at 440 kPa, small microhemorrhages (< 10 μm) were visible in the choroid plexus and near the lateral ventricles on histological sections (Fig. 4.C-D). These lesions were not detectable in T_2-weighted images, likely due to their sub-voxel size, ~5–20 μm in diameter (Fig. S4).

Four weeks post-initial FUS, ventricular enlargement could be observed in T_2-weighted and H&E images (Fig. 4.E). A significant increase in ventricle size (+70 %) was detected in the ipsilateral hemisphere in the 8-FUS group at 390 kPa, compared to the contralateral side. An increase was also visible in the 8-FUS group at 440 kPa, but did not demonstrate significant differences. Notably, one animal in the single-FUS group and one animal in the 4-FUS group at 390 kPa also showed marked ventricular enlargement in ipsilateral and contralateral hemispheres, likely reflecting spontaneous ventriculomegaly, a phenomenon previously reported in this rat strain [64].

ADC maps acquired after the final FUS session revealed no significant difference between the ipsilateral and contralateral striatum in the 4-FUS and 8-FUS groups treated at 390 kPa. In contrast, a significant reduction of 3 % and 7 % in ADC was observed in the ipsilateral striatum of animals treated with 440 kPa in both the 4-FUS and 8-FUS groups, relative to the contralateral side, respectively (Fig. 5.C). These results suggest that higher ultrasonic pressure, rather than repeated treatment alone, may contribute to the formation of transient edema in the targeted brain region. After the last FUS, we measured a 9 % decrease in the ipsilateral region between the 4-FUS at 390 kPa and the 8-FUS at 440 kPa (from 760 ± 52 to 692 ± 28 $\mu m^2/s$, respectively) and a 4 % decrease in the contralateral region (from 778 ± 58 to 746 ± 63 $\mu m^2/s$, respectively) (Table S1).

Since USPIO nanoparticles were administered within one-hour post-FUS (after 59 min on average) and have a long plasmatic half-life (~4 h30) [65], their potential extravasation into brain tissue could influence MRI signal characteristics [66,67]. To evaluate this, QSM was performed. Across all groups and timepoints, mean QSM values in the striatum showed no significant differences between the ipsilateral and contralateral hemispheres (Fig. 5.D).

Further decomposition of QSM signals into paramagnetic and diamagnetic components revealed no significant differences between ipsi and contralateral striatum (Fig. 5.*E*-F). Both positive and negative susceptibility contributions remained balanced, indicating that any USPIO extravasation likely occurred in minimal amounts and did not markedly alter local magnetic susceptibility.

Taken together, these results suggest that while increased pressure may induce mild edema detectable by diffusion MRI, repeated BBB opening at 390 kPa does not alter tissue integrity. Regarding imaging methodology, no USPIO-related artifacts were detected, suggesting that USPIO does not extravasate when injected ~60 min after BBB opening. Therefore, one can reliably use USPIO to characterize the microvascularization after FUS, as performed in this study.

3.3. Longitudinal evaluation of hemodynamic and tissue microstructure parameters following FUS sessions

Quantitative maps of CBF, R, Vf and SO_2 were obtained after FUS to assess hemodynamic and microstructural changes. These analyses focused on the striatum in the ipsilateral hemisphere, the primary target of ultrasound-mediated permeabilization, and were compared to the contralateral striatum as a control. At 30 min post-FUS, we consistently observed a reduction in cerebral perfusion in the ipsilateral striatum following BBB permeabilization at both 390 kPa and 440 kPa, with decrease of 12 ± 9 % and 17 ± 13 %, respectively, consistent with previous reports [6,11]. Over the entire experimental timeline, no substantial change in the magnitude of perfusion reduction was observed (Fig. 6.B.i).

R and Vf exhibited minimal alterations in the ipsilateral striatum compared to the contralateral hemisphere. No significant differences were observed between experimental groups or across timepoints. Of note, the ratio of the ipsilateral to the contralateral for R was found to be higher than the coefficient of variation of the measure for the 8-FUS group at 440 kPa by the end of the study (Fig. 6.B.ii–iii). In addition, values were found higher in the ipsilateral ROI compared to the contralateral (Fig. 6.C.ii-iii).

The longitudinal evolution of SO_2 (Fig. 6.B.iv) showed a gradual

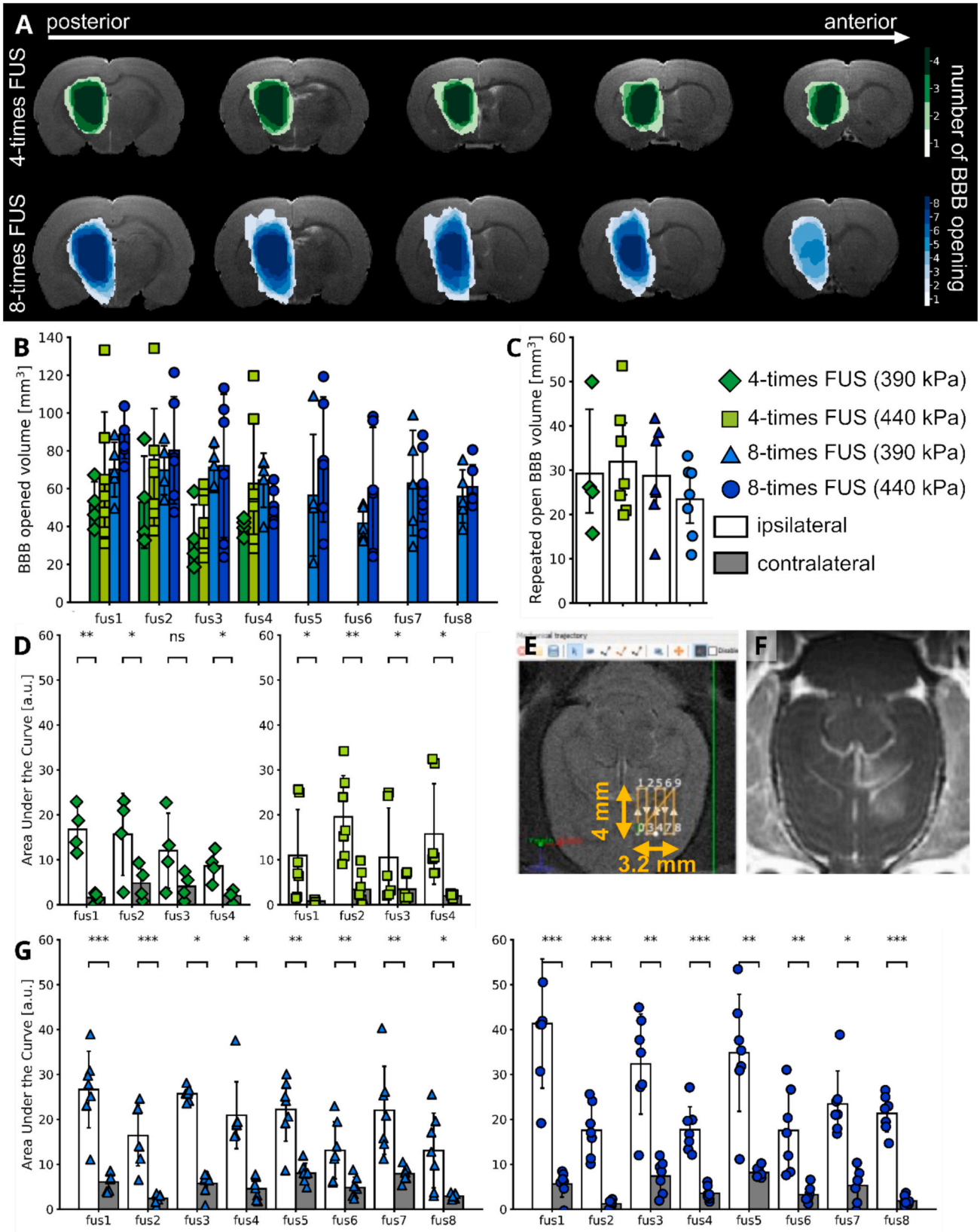

Fig. 3. Spatial and quantitative evaluation of BBB permeability after repeated FUS sessions. A) Overlay maps showing repeated BBB opening across the antero-posterior axis in representative animals from the 4-FUS (top row, green) and 8-FUS (bottom row, blue) groups. Warmer colors indicate regions of repeated BBB opening. B) Quantification of open BBB volume following each FUS session (fus1–fus8) in 4- and 8-FUS groups at 390 and 440 kPa. C) Repeated open BBB volume across all sessions showed no significant differences between groups (one-way Anova comparison; ns: not significant). (D, G) AUC values in the ipsilateral (white) and contralateral (gray) hemispheres for each FUS session (two-tailed paired Wilcoxon signed-rank test comparison; $*p < 0.05$, $**p < 0.01$, $***p < 0.001$, ns: not significant). E) MRI-based targeting schematic showing the grid of FUS trajectories and spatial coordinates (spacing of 4 mm antero-posterior and 3.2 mm mediolateral). F) Representative axial T_1-weighted MRI image post-contrast confirming BBB opening in the targeted region. Data are presented as mean ± SD.

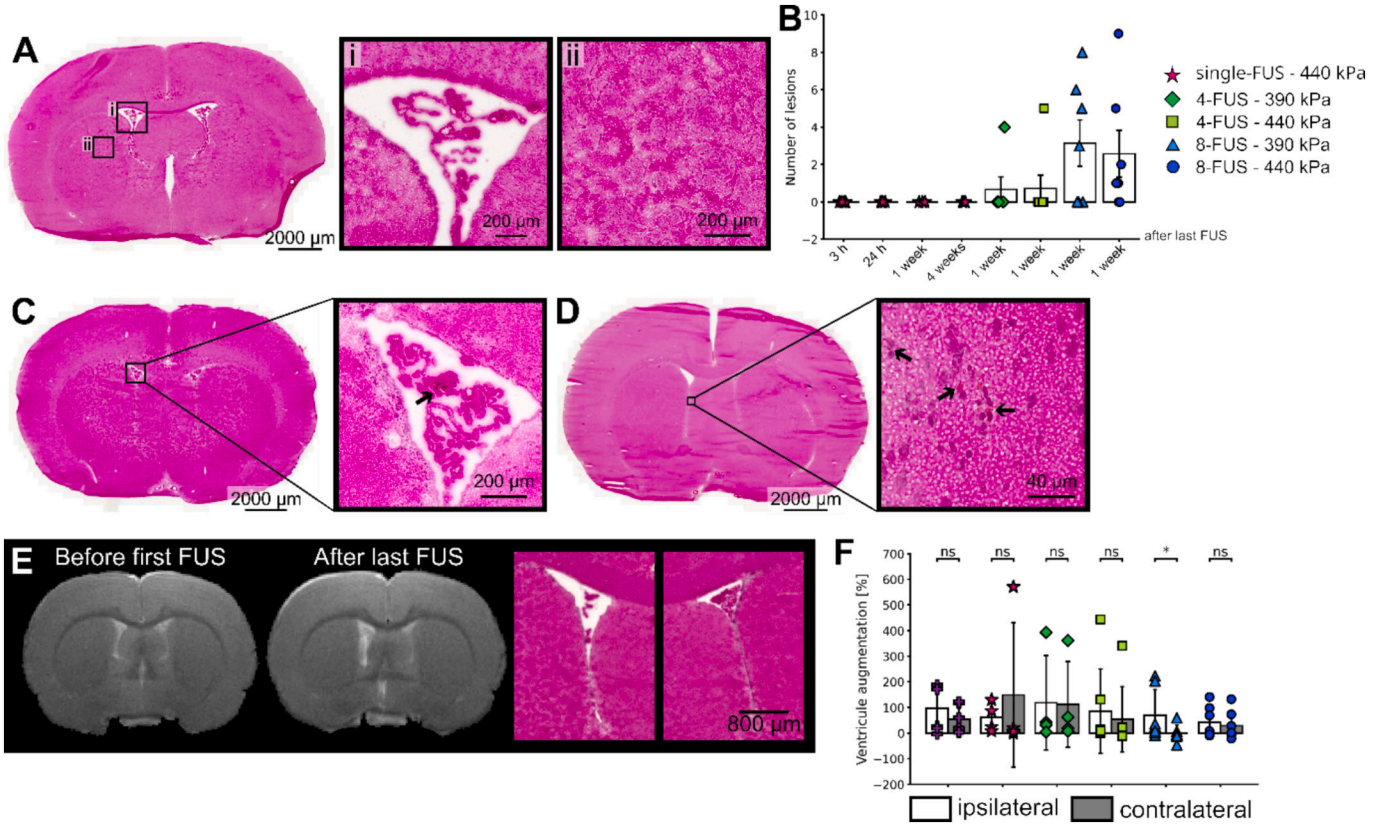

Fig. 4. Histological evaluation of brain tissue integrity and ventricle size. A) H&*E*-stained brain section acquired 3 h after a single-FUS at 440 kPa. Insets show (i) the choroid plexus within the lateral ventricle and (ii) the striatum, with no evidence of tissue damage or hemorrhagic lesions. B) Quantification of the lesion number in the choroid plexus across time points for all groups. A significant increase in lesions is observed at 4 weeks in the 8-times-FUS groups, particularly at 440 kPa. (C-D) Representative H&E sections from brains collected 1 week after 8-FUS at 440 kPa. C) Micrograph and inset show small micro-hemorrhage in the choroid plexus (black arrow). D) Micrograph and inset highlight focal micro-hemorrhages (black arrows) in the periventricular region. E) MRI observation of ventricle size before the first FUS and after the last FUS procedure (left). H&E (right) images one week after the last FUS procedure. F) Quantification of ventricle enlargement, presented as percentage of change after 4 weeks for ipsilateral and contralateral ventricles (two-tailed paired Wilcoxon signed-rank test comparison; $*p < 0.05$, ns: not significant). Data are presented as mean ± SD.

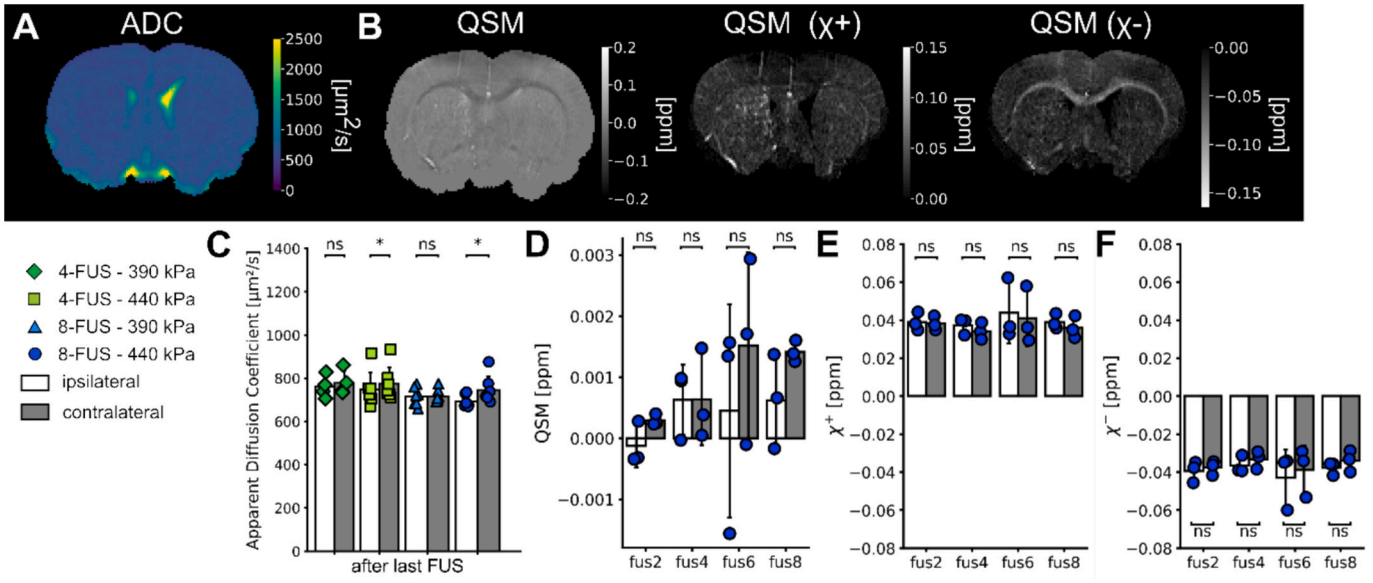

Fig. 5. ADC and QSM after 8 FUS sessions. A) Representative ADC map from a coronal brain section, showing bilateral striatal regions after 8 FUS sessions. B) QSM analysis on the same section, illustrating total susceptibility (QSM), and decomposition into paramagnetic (χ^+) and diamagnetic (χ^-) contributions. C) Quantification of ADC values in the ipsilateral and contralateral striatum across groups: 4-FUS and 8-FUS at 390 kPa and 440 kPa (two-tailed paired test comparison, $*p < 0.05$, ns: not significant). Mean susceptibility values extracted for total QSM maps (D), paramagnetic (χ^+, E), and diamagnetic (χ^-, F) components across different FUS sessions (fus2 to fus8) for 8-FUS group at 440 kPa (two-tailed paired Wilcoxon signed-rank test comparison, ns: not significant). Data are presented as mean ± SD.

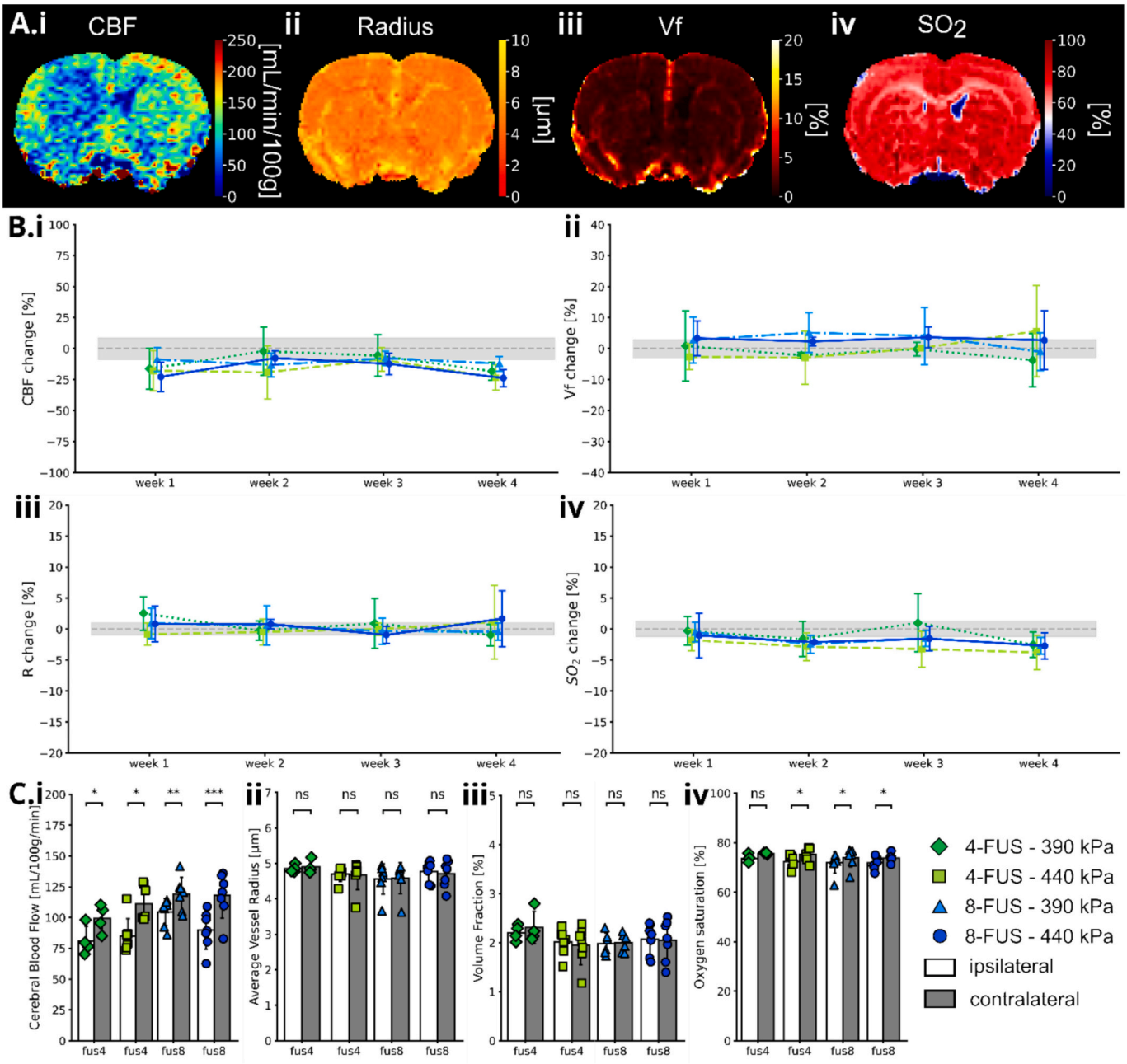

Fig. 6. Microvascular parametric mapping following repeated FUS-mediated BBB opening. A) Representative coronal parametric maps of CBF (i), R (ii), Vf (iii) and SO_2 (iv). B) Longitudinal analysis of ipsilateral-to-contralateral striatum ratios for CBF (i), R (ii), Vf (iii) and SO_2 (iv) across four weeks, following repeated FUS exposures. The shaded gray area represents the coefficient of variation for each parameter in the non-treated striatum. C) Bar plots showing absolute values of vascular parameters CBF (i), R (ii), Vf (iii) and SO_2 (iv) in ipsilateral and contralateral striatum after the last FUS session for 4-FUS and 8-FUS groups (two-tailed paired Wilcoxon signed-rank test comparison; $^*p < 0.05$, $^{**}p < 0.01$, $^{***}p < 0.001$, ns: not significant). Data are presented as mean ± SD.

decline of the ipsilateral/contralateral ratio over time. A significant reduction in SO_2 was observed specifically in the 8-FUS group at 390 kPa. Absolute values recorded after the final FUS session further confirmed a reduction in oxygen saturation in the ipsilateral striatum relative to the contralateral side (4-FUS – 390 kPa, -2.5 %, $p = 0.096$; 4-FUS – 440 kPa, -3.8 %, $p = 0.012$; 8-FUS – 390 kPa, -2.7 %, $p = 0.016$; 8-FUS – 440 kPa, -2.7 %, $p = 0.015$; Fig. 6.C.iv). A summary of CBF, R, Vf, and SO_2 measurements following the final FUS session is provided in Table S1.

3.4. Histological analysis

We performed GFAP immunostaining to evaluate astrocytic reactivity across different treatment regimens. Whole-brain coronal sections (Fig. 7.A) and higher-magnification images (Fig. 7.B) revealed marked differences in GFAP expression depending on the number of FUS sessions and applied acoustic pressure.

In the 4-FUS group at 390 kPa, GFAP staining appeared largely comparable between the ipsilateral and contralateral hemispheres, indicating minimal glial activation. At 440 kPa, a subtle increase in GFAP signal was observed in the treated hemisphere, suggesting a modest astrocytic response. In contrast, animals from the 8-FUS groups exhibited more pronounced astrocytic labeling, particularly at 440 kPa, where dense and hypertrophic GFAP-positive processes were clearly visible in the ipsilateral hemisphere.

These visual observations were confirmed by quantitative analyses of

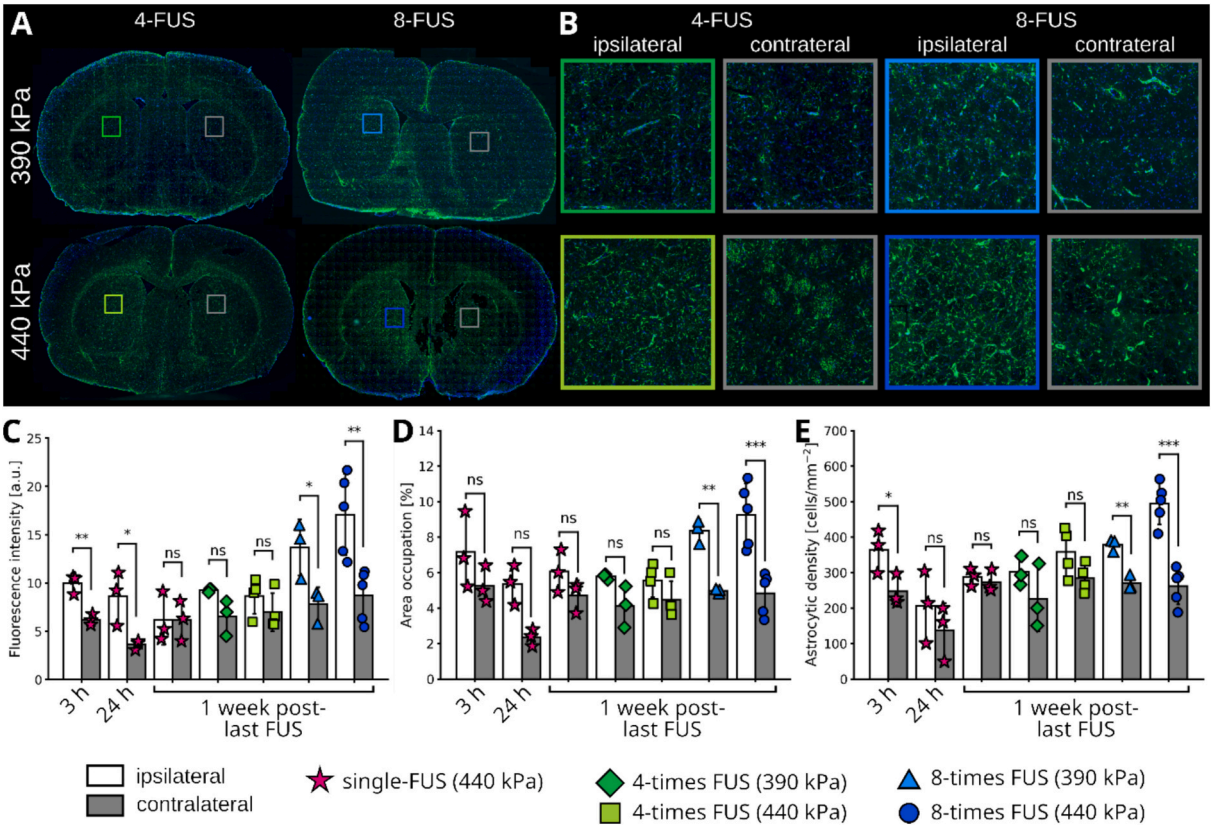

Fig. 7. Quantification of astrocytic marker following FUS-induced BBB opening. A) Representative immunofluorescence image of coronal brain sections for the different groups, illustrating the regions of interest (ROIs) for analysis. Ipsilateral (colored square) within the open BBB region and contralateral (gray square) regions were selected for quantification. Astrocytes are labeled in green (GFAP) and nuclei in blue (DAPI). Image analysis quantification of mean fluorescence intensity (C), area occupation (D) and astrocytic density (E) of GFAP staining in ipsilateral (white bar) and contralateral (gray bar) regions across different FUS regimens: 3 h, 24 h and 1 week after single-FUS at 440 kPa (pink star), and 1 week after the last FUS session for the 4-times-FUS at 390 kPa (diamonds), 4-times-FUS at 440 kPa (squares), 8-times-FUS at 390 kPa (triangles), and 8-times-FUS at 440 kPa (circles) groups (two-tailed paired Wilcoxon signed-rank test comparison, $*p < 0.05$, $**p < 0.01$, $***p < 0.001$, ns = not significant). Data are presented as mean ± SD. (For interpretation of the references to colour in this figure legend, the reader is referred to the web version of this article.)

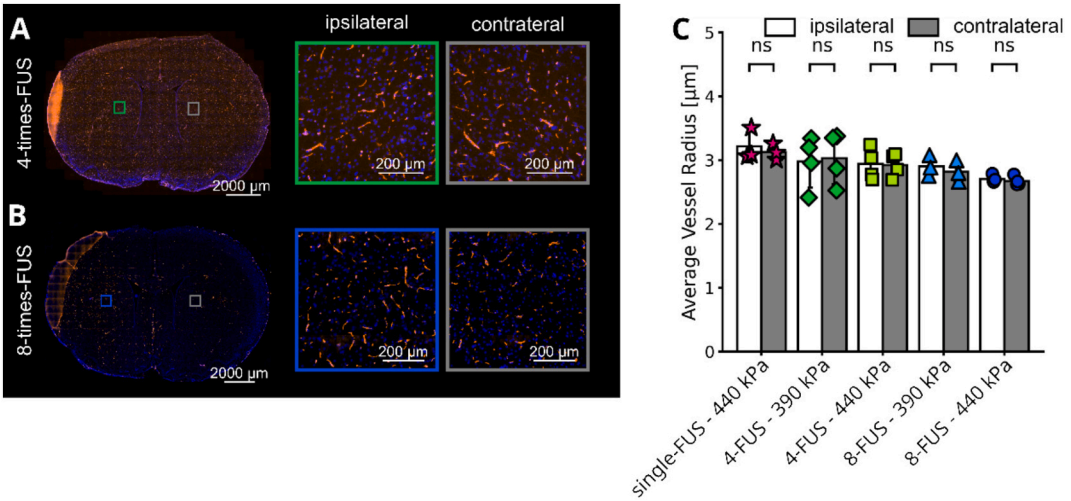

Fig. 8. Histological analysis of vessels following repeated FUS sessions. (A–B) Representative coronal brain sections showing immunolabeled blood vessels (orange, lectin) and nuclei (blue, DAPI) from animals treated with either (A) 4-times-FUS or (B) 8-times-FUS. Ipsilateral (treated) and contralateral (untreated) regions of interest are highlighted and shown at higher magnification. C) Quantification of average vessel radius in the ipsilateral and contralateral hemispheres across different FUS regimens one week after the last FUS session: single-FUS at 440 kPa (stars), 4-times-FUS at 390 kPa (diamonds), 4-times-FUS at 440 kPa (squares), 8-times-FUS at 390 kPa (triangles), and 8-times-FUS at 440 kPa (circles) (two-tailed paired Wilcoxon signed-rank test comparison, ns: not significant). Data are presented as mean ± SD. (For interpretation of the references to colour in this figure legend, the reader is referred to the web version of this article.)

fluorescence intensity, astrocyte density, and GFAP-positive area occupation (Fig. 7.C–E). In the acute phase (3 h and 24 h post single-FUS at 440 kPa), we observed increases in fluorescence intensity (1.61-fold, $p = 5 \times 10^{-3}$ at 3 h; 2.39-fold, $p = 0.04$ at 24 h), astrocyte density (1.47-fold, $p = 0.03$ at 3 h; 1.51-fold, $p = 0.06$ at 24 h) and percentage of area occupation (1.36-fold, $p = 0.16$ at 3 h; 2.27-fold, $p = 0.08$ at 24 h) in the treated hemisphere, indicating a rapid astrocytic response. One week after the final FUS procedure, we did not observe any astrocytic activation in the single-FUS group at 440 kPa (1.01-fold in fluorescence intensity, 1.05-fold in astrocytic density and 1.29-fold in percentage of area occupation). Thus, glial reactivity fades within a week following the FUS session at the highest pressure. In the 4-FUS groups (390 and 440 kPa), astrocytic activation remained minimal, with no significant differences compared to the contralateral side, suggesting that glial reactivity fades between weekly sessions with possibly the same dynamic as the one observed in the single-FUS group.

In contrast, animals in the 8-FUS groups demonstrated significantly elevated fluorescence intensity (1.75-fold, $p = 0.04$ at 390 kPa; 1.96-fold, $p = 5 \times 10^{-3}$ at 440 kPa), area occupation (1.67-fold $p = 0.008$ and 1.92-fold, $p = 10^{-4}$), and astrocyte density (1.4-fold, $p = 8 \times 10^{-3}$ and 1.89-fold, $p = 1.4 \times 10^{-6}$), indicating a persistent astrocytic response under more intensive treatment conditions. Together, these findings highlight the importance of treatment frequency and pressure in shaping the astrocytic landscape post-FUS, with more frequent and intense regimens leading to sustained glial activation.

The histological analysis of SMI71-immunolabeled vessels (Fig. 8) revealed microvascular alterations following repeated FUS-mediated BBB opening. In the different groups, no significant differences were observed between ipsilateral and contralateral striatum. However, after 8 FUS sessions, a small increase (~3 %, non-significant) in the ipsilateral region was measured (Fig. 8.C). One can see the decrease in overall values measured in both ipsilateral and contralateral regions with the increase of treatment repetition and acoustic pressure. In Fig. S5, the heatmap represents the decrease in vessel radius measured in both regions across groups, for the ipsi and contralateral regions. We measured a decrease of 9 to 12 % between the 4-times-FUS group at 390 kPa and the 8-times-FUS group at 440 kPa. These changes may reflect an adaptive structural response to repeated mechanical stress, or early indicators of vascular fatigue. Notably, a slight reduction in vessel diameter was also observed in the contralateral hemisphere of some groups, which could be linked to systemic effects such as repeated anesthesia exposure. Altogether, these findings underscore the importance of monitoring vascular integrity in chronic FUS protocols and warrant further investigation into potential systemic and long-term effects.

4. Discussion and conclusion

In this study, we performed a longitudinal assessment in healthy rats of the microvascular and glial responses to repeated MR-guided FUS-induced BBB opening. Weekly BBB permeabilization at moderate acoustic pressures was found to be feasible and well tolerated. However, increasing either the frequency of BBB permeabilization or the applied acoustic pressure induced measurable biological effects, highlighting the importance of optimizing treatment protocols considering the risk versus benefit for future clinical translation. In particular, the results of current research into the prevention of neuroinflammation during surgery could be useful in the context of the FUS-induced BBB opening [68].

Using a raster scan approach combined with MRI guidance, BBB opening was reproducible across sessions. Yet, low inter-animal variability was observed and could be ascribed to slight variations in the positioning of the animal in the MRgFUS which alters FUS transmission across the skull. DCE-MRI confirmed stable contrast agent extravasation, i.e. stable BBB permeability, over the course of the experiments. Our results are consistent with previous findings showing that large-volume BBB opening does not delay closure under moderate acoustic conditions [69] and confirm that repeated and large-volume BBB opening does not compromise BBB permeability.

No important macroscopic tissue damage such as hemorrhage or edema was detected, contrasting with prior studies where repeated FUS sessions led to structural alterations visible both in T_2*-weighted image and H&E staining [32,33]. These alterations were most likely due to higher microbubble doses and the absence of cavitation level control. In our protocol, the use of a microbubble dose previously validated for cavitation-controlled BBB opening at the MI values used in this study (0.32–0.37) [6] and in agreement with established safety thresholds [70] contributed to the preservation of vascular integrity. However, subtle cumulative effects, such as small petechial hemorrhages, were occasionally detected using histology (Fig. 4.B), raising concerns about potential long-term consequences of repeated BBB permeabilization. In particular, the choroid plexus plays an important role in brain regulation [71] and the microbleeds observed in these fragile structures should not be considered lightly. These findings reinforce the need for implementing closed-loop cavitation control even in preclinical studies [72]. From a morphological perspective, ventricular enlargement was observed after repeated FUS sessions, consistent with previous reports [33,73]. Although these enlargements could be ascribed to spontaneous ventriculomegaly, a phenomenon already described in the rat strain used in this study [64]. Interestingly, a similar ventricular enlargement has also been reported in a trauma model of repeated mild concussive impacts in rats, further suggesting that repeated mechanical stress—even at sub-injury levels—can alter ventricular morphology [74].

Despite the absence of overt damage, consistent vascular responses were detected after each FUS procedure. CBF measured about 30 min post-FUS in our protocol was reduced by approximately 15 % in the targeted region. This perfusion drop remained stable across sessions, independently of acoustic pressure or the volume of the permeabilized BBB. These findings are consistent with previous reports describing transient CBF reductions following single FUS-induced BBB opening [6,11]. We also observed that the volume with reduced CBF was larger than the volume with permeabilized BBB, as previously reported [6], but this point was not quantified in this study. These observations suggest that CBF reduction is an acute, transient, physiological response to FUS that is not amplified by treatment repetition under the conditions tested.

At the microvascular level, a trend towards a small increase of Vf and R was observed (Fig. 6.B.ii-iii, Fig. 8.C). As contralateral and ipsilateral areas exhibited similar reductions and as this reduction was more pronounced in the 8-FUS group, this trend should rather be ascribed to repeated anesthesia than to repeated BBB opening. This is in accordance with a trend in Vf reduction previously observed in another animal model that underwent repeated anesthesia [75]. Conversely, the reduction in SO_2 detected in the ipsilateral side only may be related to repeated BBB opening rather than to repeated anesthesia. As CBF and Vf ipsilateral to contralateral ratio remained stable, this reduction in SO_2 could be ascribed to a slight increase in the tissue cerebral metabolic rate of oxygen. Altogether, the microvascularization appears robust to repeated BBB opening.

The astrocytic response observed in this study may be ascribed to both anesthesia and FUS. Regarding anesthesia, it is known that isoflurane induces an astrocytic response [76–78]. Accordingly, we observed in the contralateral area an increasing astrocytic reactivity between single-FUS, 4-FUS, and 8-FUS (Fig. 7.C). However, the difference in astrocytic reactivity between ipsilateral and contralateral areas may rather be ascribed to FUS. Histological staining revealed an astrocytic differential activation as early as 3 h post-FUS (~1.6-fold between ipsi- and contralateral areas), followed by an increased differential activation at 24 h (~2.4-fold), in agreement with previous studies that reported transient GFAP upregulation between 24 and 48 h following single FUS exposure and using similar MI and microbubble doses [6,13,17,79]. One week after a single-FUS session, astrocytic markers returned to baseline levels, confirming the transient nature of the glial

response, as previously described [6]. Regarding multiple FUS sessions, histological staining performed one week after the last FUS session revealed limited differential astrocytic activation in the 4-FUS group (∼1.2-fold), but significant astrogliosis in the 8-FUS group, particularly at higher acoustic pressures (∼2-fold). Previous studies similarly reported astrocytic activation following weekly FUS sessions [32,33]. These results provide evidence that repeated BBB opening can induce a cumulative neuroimmune response. While our data are in line with previous literature, the non-exhaustive list of studies reporting GFAP outcomes after FUS (Table S2) illustrates the heterogeneity of findings and the need for standardized timepoints and protocols to define methods that limit these inflammatory processes known to be involved in the progression of neurodegenerative diseases or in tumor-associated brain remodeling [80].

This study has several limitations. Behavioral and cognitive impacts were not assessed, and future work should examine social interaction, anxiety, and locomotor activity, at short and long delays after repeated FUS. Given known regional heterogeneities in BBB structure and neurovascular-unit composition, the vulnerability to repeated FUS may vary across brain areas, a factor warranting future region-specific investigations, as briefly observed in previous studies [32,33]. Long anesthesia was performed to access multiparametric MRI imaging. The use of anesthesia, known to alter CBF and $CMRO_2$ [81], could have masked subtle hypoxic effects. Other studies should also evaluate repeated BBB opening with shorter and other types of anesthesia as well as potential systemic immune response and cytokines production [15,82,83]. Regarding the clinical translation of FUS-mediated BBB opening, we recommend paying attention to both the impact of FUS on microvascularization and on brain tissue inflammation. Finally, cavitation monitoring was not performed mainly to the challenge faced with continuous FUS pulses along with a moving transducer; integrating acoustic feedback could optimize future treatments to further minimize risks and possibly better control tissue inflammation.

In conclusion, weekly FUS-induced BBB opening at moderate pressures appears safe in healthy rat brain tissue, with minimal microvascular and neuroinflammatory effects. However, increasing the treatment frequency to twice per week induces mild but detectable biological responses, emphasizing that FUS protocols must be optimized carefully according to the clinical indication and therapeutic target to minimize side effects. Acoustic pressures should be kept as low as feasible to preserve microvascular function over repeated sessions.

CRediT authorship contribution statement

Sébastien Rigollet: Writing – review & editing, Writing – original draft, Visualization, Validation, Software, Resources, Project administration, Methodology, Investigation, Formal analysis, Data curation, Conceptualization. **Aurélien Delphin:** Software, Resources, Methodology. **Lucie Chalet:** Software, Resources, Methodology, Formal analysis. **Thomas Ador:** Validation, Resources. **Erik Dumont:** Supervision, Resources, Funding acquisition. **Benjamin Lemasson:** Software, Resources, Funding acquisition. **Thomas Christen:** Software, Resources, Funding acquisition. **Chantal Pichon:** Supervision, Resources, Funding acquisition. **Anthony Delalande:** Writing – review & editing, Validation, Supervision, Resources, Methodology, Funding acquisition, Conceptualization. **Vasile Stupar:** Writing – review & editing, Validation, Supervision, Resources, Methodology, Funding acquisition, Conceptualization. **Emmanuel L. Barbier:** Writing – review & editing, Validation, Supervision, Methodology, Funding acquisition, Conceptualization.

Fundings

This work was performed on the IRMaGe platform member of France Life Imaging network (grant ANR-11-INBS-0006). Part of the FUS equipment was sponsored by the Fédération pour la Recherche sur le Cerveau (FRC) and the Rotary club. This research was partly funded by ANR FUSBRAIN (Grant ANR-21-18CE-0019), technological maturation project funded by C-Valo (PIA FNV Grant ANR-17-SATE-0003). This work was supported by the Photonic Imaging Center of Grenoble Institute Neuroscience (Univ Grenoble Alpes – Inserm U1216) which is part of the ISdV core facility and certified by the IBiSA label.

Declaration of competing interest

S.R. is employed by Image Guided Therapy company. E. D. owns the Image Guided Therapy company. A.D. is co-founder of the company Harmonix. A.D. and C.P. are co-inventors of the patent “lipid microbubbles for the targeted delivery of active agents” WO2023237842 (A1). The other authors declare no other conflict of interest.

Acknowledgments

The authors thank Nora Collomb for her assistance during the in vivo experiments. Qendresa Arifi and Thaïs La Rocca for realizing part of the histological staining. The authors are also grateful to the animal facility working team for their assistance in animal care and housing at the Grenoble Institut des Neurosciences animal facility.

Appendix A. Supplementary data

Supplementary data to this article can be found online at https://doi.org/10.1016/j.jconrel.2025.114151.

Data availability

Data will be made available on request.

References

[1] K. Kisler, A.R. Nelson, A. Montagne, B.V. Zlokovic, Cerebral blood flow regulation and neurovascular dysfunction in Alzheimer disease, Nat Rev Neurosci [Internet]. 18 (2017) 419–434 [cited 18 July 2024]. Available at: https://www.nature.com/articles/nrn.2017.48.

[2] S. Bae, K. Liu, A.N. Pouliopoulos, R. Ji, S. Jiménez-Gambín, O. Yousefian, et al., Transcranial blood-brain barrier opening in Alzheimer’s disease patients using a portable focused ultrasound system with real-time 2-D cavitation mapping, Theranostics 14 (2024) 4519–4535.

[3] A. Carpentier, R. Stupp, A.M. Sonabend, H. Dufour, O. Chinot, B. Mathon, et al., Repeated blood–brain barrier opening with a nine-emitter implantable ultrasound device in combination with carboplatin in recurrent glioblastoma: a phase I/II clinical trial, Nat Commun [Internet]. 15 (2024) 1650 [cited 22 March 2024]. Available at: https://www.nature.com/articles/s41467-024-45818-7.

[4] A.R. Rezai, P.-F. D’Haese, V. Finomore, J. Carpenter, M. Ranjan, K. Wilhelmsen, et al., Ultrasound Blood–Brain Barrier Opening and Aducanumab in Alzheimer’s Disease, N Engl J Med [Internet] 390 (2024) 55–62 [cited 22 March 2024]. Available at: http://www.nejm.org/doi/10.1056/NEJMoa2308719.

[5] Y. Meng, R.M. Reilly, R.C. Pezo, M. Trudeau, A. Sahgal, A. Singnurkar, et al., MR-guided focused ultrasound enhances delivery of trastuzumab to Her2-positive brain metastases, Sci Transl Med [Internet]. 13 (2021) [cited 22 March 2024]. eabj4011. Available at: https://www.science.org/doi/10.1126/scitranslmed.abj4011.

[6] S. Rigollet, C. Rome, T. Ador, E. Dumont, C. Pichon, A. Delalande, et al., FUS-mediated BBB opening leads to transient perfusion decrease and inflammation without acute or chronic brain lesion, Theranostics 14 (2024) 4147–4160.

[7] S.B. Raymond, J. Skoch, K. Hynynen, B.J. Bacskai, Multiphoton imaging of ultrasound/optison mediated cerebrovascular effects *in vivo*, J Cereb Blood Flow Metab [Internet] 27 (2007) 393–403 [cited 14 September 2022]. Available at: http://journals.sagepub.com/doi/10.1038/sj.jcbfm.9600336.

[8] E.E. Cho, J. Drazic, M. Ganguly, B. Stefanovic, K. Hynynen, Two-Photon Fluorescence Microscopy Study of Cerebrovascular Dynamics in Ultrasound-Induced Blood—Brain Barrier Opening, J Cereb Blood Flow Metab [Internet] 31 (2011) 1852–1862 [cited 14 September 2022]. Available at: http://journals.sagepub.com/doi/10.1038/jcbfm.2011.59.

[9] N. Todd, Y. Zhang, M. Livingstone, D. Borsook, N. McDannold, The neurovascular response is attenuated by focused ultrasound-mediated disruption of the blood-brain barrier, NeuroImage [Internet] 201 (2019) [cited 17 February 2022]. 116010. Available at: https://linkinghub.elsevier.com/retrieve/pii/S1053811919305919.

[10] N. Todd, Y. Zhang, M. Arcaro, L. Becerra, D. Borsook, M. Livingstone, et al., Focused ultrasound induced opening of the blood-brain barrier disrupts inter-hemispheric resting state functional connectivity in the rat brain, NeuroImage

[Internet] 178 (2018) 414–422 [cited 31 January 2023]. Available at: https://linkinghub.elsevier.com/retrieve/pii/S1053811918304877.
[11] W. Labriji, J. Clauzel, J. Mestas, M. Lafond, C. Lafon, A. Salabert, et al., Evidence of cerebral hypoperfusion consecutive to ultrasound-mediated blood-brain barrier opening in rats, Magn Reson Med [Internet] 89 (6) (2023) 2281–2294 [cited 31 January 2023]. mrm.29596. Available at: https://onlinelibrary.wiley.com/doi/10.1002/mrm.29596.
[12] N. Todd, C. Angolano, C. Ferran, A. Devor, D. Borsook, N. McDannold, Secondary effects on brain physiology caused by focused ultrasound-mediated disruption of the blood–brain barrier, J Control Release [Internet]. 324 (2020) 450–459 [cited 27 October 2022]. Available at: https://linkinghub.elsevier.com/retrieve/pii/S0168365920303175.
[13] Z.I. Kovacs, S. Kim, N. Jikaria, F. Qureshi, B. Milo, B.K. Lewis, et al., Disrupting the blood–brain barrier by focused ultrasound induces sterile inflammation, Proc Natl Acad Sci USA [Internet] 114 (2017) [cited 10 January 2023]. Available at: https://pnas.org/doi/full/10.1073/pnas.1614777114.
[14] D. McMahon, R. Bendayan, K. Hynynen, Acute effects of focused ultrasound-induced increases in blood-brain barrier permeability on rat microvascular transcriptome, Sci Rep [Internet] 7 (2017) 45657 [cited 16 August 2024]. Available at: https://www.nature.com/articles/srep45657.
[15] R. Ji, M.E. Karakatsani, M. Burgess, M. Smith, M.F. Murillo, E.E. Konofagou, Cavitation-modulated inflammatory response following focused ultrasound blood-brain barrier opening, J. Control. Release 337 (2021) 458–471.
[16] C. Poon, C. Pellow, K. Hynynen, Neutrophil recruitment and leukocyte response following focused ultrasound and microbubble mediated blood-brain barrier treatments, Theranostics [Internet]. 11 (2021) 1655–1671 [cited 25 February 2024]. Available at: https://www.thno.org/v11p1655.htm.
[17] C.M. Gorick, A.S. Mathew, W.J. Garrison, E.A. Thim, D.G. Fisher, C.A. Copeland, et al., Sonoselective transfection of cerebral vasculature without blood–brain barrier disruption, Proc Natl Acad Sci U S A [Internet] 117 (2020) 5644–5654 [cited 21 May 2021]. Available at: http://www.pnas.org/lookup/doi/10.1073/pnas.1914595117.
[18] P.J. Martinez, J.J. Song, F.G. Garay, K.-H. Song, T. Mufford, J. Steiner, et al., Comprehensive assessment of blood–brain barrier opening and sterile inflammatory response: unraveling the therapeutic window, Sci Rep [Internet]. 14 (2024) 17036 [cited 11 September 2024]. Available at: https://www.nature.com/articles/s41598-024-67916-8.
[19] M. Aryal, N. Vykhodtseva, Y.-Z. Zhang, J. Park, N. McDannold, Multiple treatments with liposomal doxorubicin and ultrasound-induced disruption of blood–tumor and blood–brain barriers improve outcomes in a rat glioma model, J Control Release [Internet] 169 (2013) 103–111 [cited 5 April 2022]. Available at: https://linkinghub.elsevier.com/retrieve/pii/S0168365913002149.
[20] N. McDannold, Y. Zhang, J.G. Supko, C. Power, T. Sun, C. Peng, et al., Acoustic feedback enables safe and reliable carboplatin delivery across the blood-brain barrier with a clinical focused ultrasound system and improves survival in a rat glioma model, Theranostics [Internet] 9 (2019) 6284–6299 [cited 6 November 2023]. Available at: http://www.thno.org/v09p6284.htm.
[21] S.H. Park, M.J. Kim, H.H. Jung, W.S. Chang, H.S. Choi, I. Rachmilevitch, et al., Safety and feasibility of multiple blood-brain barrier disruptions for the treatment of glioblastoma in patients undergoing standard adjuvant chemotherapy, J. Neurosurg. [Internet] 134 (2021) 475–483 [cited 4 April 2022]. Available at: https://thejns.org/view/journals/j-neurosurg/134/2/article-p475.xml.
[22] A.M. Sonabend, A. Gould, C. Amidei, R. Ward, K.A. Schmidt, D.Y. Zhang, et al., Repeated blood–brain barrier opening with an implantable ultrasound device for delivery of albumin-bound paclitaxel in patients with recurrent glioblastoma: a phase 1 trial, The Lancet Oncology [Internet]. 24 (2023) 509–522 [cited 21 July 2023]. Available at: https://linkinghub.elsevier.com/retrieve/pii/S1470204523001122.
[23] A. Idbaih, M. Canney, L. Belin, C. Desseaux, A. Vignot, G. Bouchoux, et al., Safety and Feasibility of Repeated and Transient Blood–Brain Barrier Disruption by Pulsed Ultrasound in Patients with Recurrent Glioblastoma, Clin Cancer Res [Internet] 25 (2019) 3793–3801 [cited 4 April 2022]. Available at: http://clincancerres.aacrjournals.org/lookup/doi/10.1158/1078-0432.CCR-18-3643.
[24] R. Pandit, G. Leinenga, J. Götz, Repeated ultrasound treatment of tau transgenic mice clears neuronal tau by autophagy and improves behavioral functions, Theranostics [Internet] 9 (2019) 3754–3767 [cited 21 February 2024]. Available at: http://www.thno.org/v09p3754.htm.
[25] Y. Shen, L. Hua, C.-K. Yeh, L. Shen, M. Ying, Z. Zhang, et al., Ultrasound with microbubbles improves memory, ameliorates pathology and modulates hippocampal proteomic changes in a triple transgenic mouse model of Alzheimer's disease, Theranostics [Internet] 10 (2020) 11794–11819 [cited 21 September 2023]. Available at: https://www.ncbi.nlm.nih.gov/pmc/articles/PMC7546002/.
[26] G. Leinenga, J. Götz, Safety and efficacy of scanning ultrasound treatment of aged APP23 mice, Front. Neurosci. 12 (2018) 55.
[27] M.E. Karakatsani, T. Kugelman, R. Ji, M. Murillo, S. Wang, Y. Niimi, et al., Unilateral focused ultrasound-induced blood-brain barrier opening reduces phosphorylated Tau from the rTg4510 mouse model, Theranostics [Internet] 9 (2019) 5396–5411 [cited 5 April 2022]. Available at: http://www.thno.org/v09p5396.htm.
[28] S. Epelbaum, N. Burgos, M. Canney, D. Matthews, M. Houot, M.D. Santin, et al., Pilot study of repeated blood-brain barrier disruption in patients with mild Alzheimer's disease with an implantable ultrasound device, Alz Res Therapy [Internet]. 14 (2022) 40 [cited 1 February 2023]. Available at: https://alzres.biomedcentral.com/articles/10.1186/s13195-022-00981-1.
[29] A.R. Rezai, M. Ranjan, M.W. Haut, J. Carpenter, P.-F. D'Haese, R.I. Mehta, et al., Focused ultrasound–mediated blood-brain barrier opening in Alzheimer's disease: long-term safety, imaging, and cognitive outcomes, J. Neurosurg. [Internet]. (2022) 1–9 [cited 25 February 2024]. Available at: https://thejns.org/view/journals/j-neurosurg/aop/article-10.3171-2022.9.JNS221565/article-10.3171-2022.9.JNS221565.xml.
[30] O.O. Olumolade, S. Wang, G. Samiotaki, E.E. Konofagou, Longitudinal motor and behavioral assessment of blood–brain barrier opening with transcranial focused ultrasound, Ultrasound Med Biol [Internet] 42 (2016) 2270–2282 [cited 6 April 2022]. Available at: https://linkinghub.elsevier.com/retrieve/pii/S0301562916300618.
[31] D.G. Blackmore, F. Turpin, A.Z. Mohamed, F. Zong, R. Pandit, M. Pelekanos, et al., Multimodal analysis of aged wild-type mice exposed to repeated scanning ultrasound treatments demonstrates long-term safety, Theranostics [Internet]. 8 (2018) 6233–6247 [cited 21 February 2024]. Available at: http://www.thno.org/v08p6233.htm.
[32] S. Sinharay, T.-W. Tu, Z.I. Kovacs, W. Schreiber-Stainthorp, M. Sundby, X. Zhang, et al., In vivo imaging of sterile microglial activation in rat brain after disrupting the blood-brain barrier with pulsed focused ultrasound: [18F]DPA-714 PET study, J. Neuroinflammation 16 (2019) 155.
[33] Z.I. Kovacs, T.-W. Tu, M. Sundby, F. Qureshi, B.K. Lewis, N. Jikaria, et al., MRI and histological evaluation of pulsed focused ultrasound and microbubbles treatment effects in the brain, Theranostics [Internet]. 8 (2018) 4837–4855 [cited 19 October 2023]. Available at: http://www.thno.org/v08p4837.htm.
[34] M.E. Downs, A. Buch, C. Sierra, M.E. Karakatsani, S. Chen, E.E. Konofagou, et al., Long-Term Safety of Repeated Blood-Brain Barrier Opening via Focused Ultrasound with Microbubbles in Non-Human Primates Performing a Cognitive Task. Liebner S, Ed, PLoS ONE [Internet] 10 (2015) [cited 4 April 2022]. e0125911. Available at: https://dx.plos.org/10.1371/journal.pone.0125911.
[35] C. Horodyckid, M. Canney, A. Vignot, R. Boisgard, A. Drier, G. Huberfeld, et al., Safe long-term repeated disruption of the blood-brain barrier using an implantable ultrasound device: a multiparametric study in a primate model, JNS [Internet] 126 (2017) 1351–1361 [cited 11 February 2022]. Available at: https://thejns.org/view/journals/j-neurosurg/126/4/article-p1351.xml.
[36] A. Delphin, F. Boux, C. Brossard, T. Coudert, J.M. Warnking, B. Lemasson, et al., Enhancing MR vascular fingerprinting with realistic microvascular geometries, Imag. Neurosci. [Internet]. 2 (2024) 1–13 [cited 28 January 2025]. Available at: https://direct.mit.edu/imag/article/doi/10.1162/imag_a_00377/125239/Enhancing-MR-vascular-Fingerprinting-with.
[37] T. Christen, N.A. Pannetier, W.W. Ni, D. Qiu, M.E. Moseley, N. Schuff, et al., MR vascular fingerprinting: a new approach to compute cerebral blood volume, mean vessel radius, and oxygenation maps in the human brain, NeuroImage [Internet]. 89 (2014) 262–270 [cited 20 November 2023]. Available at: https://linkinghub.elsevier.com/retrieve/pii/S1053811913012019.
[38] B. Lemasson, N. Pannetier, N. Coquery, L.S.B. Boisserand, N. Collomb, N. Schuff, et al., MR vascular fingerprinting in stroke and brain tumors models, Sci Rep [Internet]. 6 (2016) 37071 [cited 26 April 2023]. Available at: https://www.nature.com/articles/srep37071.
[39] C. Chevaleyre, A. Novell, N. Tournier, A. Dauba, S. Dubois, D. Kereselidze, et al., Efficient PD-L1 imaging of murine glioblastoma with FUS-aided immunoPET by leveraging FcRn-antibody interaction, Theranostics [Internet]. 13 (2023) 5584–5596 [cited 19 July 2024]. Available at: https://www.thno.org/v13p5584.htm.
[40] B.S. Owusu-Yaw, Y. Zhang, L. Garrett, A. Yao, K. Shing, A.R. Batista, et al., Focused ultrasound-mediated disruption of the blood–brain barrier for AAV9 delivery in a mouse model of Huntington's Disease, Pharm. Int. 16 (2024) 710 [cited 6 September 2024]. Available at: https://www.mdpi.com/1999-4923/16/6/710.
[41] A.W. Gorman, K.M. Deh, C.M. Schwiedrzik, J.R. White, E.V. Groman, C.A. Fisher, et al., Brain Iron distribution after multiple doses of ultra-small superparamagnetic Iron oxide particles in rats, Comp. Med. 68 (2018) 139–147.
[42] R. Magnin, F. Rabusseau, F. Salabartan, S. Mériaux, J.-F. Aubry, D. Le Bihan, et al., Magnetic resonance-guided motorized transcranial ultrasound system for blood-brain barrier permeabilization along arbitrary trajectories in rodents, J Ther Ultrasound [Internet]. 3 (2015) 22 [cited 21 May 2021]. Available at: http://www.jtultrasound.com/content/3/1/22.
[43] K.-H. Song, A.C. Fan, J.J. Hinkle, J. Newman, M.A. Borden, B.K. Harvey, Microbubble gas volume: a unifying dose parameter in blood-brain barrier opening by focused ultrasound, Theranostics [Internet]. 7 (2017) 144–152 [cited 23 July 2024]. Available at: http://www.thno.org/v07p0144.htm.
[44] T. Ador, M. Fournié, S. Rigollet, C. Counil, V. Stupar, E.L. Barbier, et al., Ultrasound-assisted blood–brain barrier opening monitoring by photoacoustic and fluorescence imaging using indocyanine green, Ultrasound Med. Biol. [Internet] 51 (2025) 1059–1069 [cited 29 May 2025]. Available at: https://linkinghub.elsevier.com/retrieve/pii/S0301562925000687.
[45] M.-S. Felix, E. Borloz, K. Metwally, A. Dauba, B. Larrat, V. Matagne, et al., Ultrasound-mediated blood-brain barrier opening improves whole brain gene delivery in mice, Pharm. Int. 13 (2021) 1245 [cited 24 January 2022]. Available at: https://www.mdpi.com/1999-4923/13/8/1245.
[46] L. Hirschler, C.S. Debacker, J. Voiron, S. Köhler, J.M. Warnking, E.L. Barbier, Interpulse phase corrections for unbalanced pseudo-continuous arterial spin labeling at high magnetic field: RF Phase Optimization for Unbalanced pCASL, Magn Reson Med [Internet] 79 (2018) 1314–1324 [cited 26 April 2023]. Available at: https://onlinelibrary.wiley.com/doi/10.1002/mrm.26767.
[47] T. Christen, P. Bouzat, N. Pannetier, N. Coquery, A. Moisan, B. Lemasson, et al., Tissue oxygen saturation mapping with magnetic resonance imaging, J Cereb Blood Flow Metab [Internet] 34 (2014) 1550–1557 [cited 16 September 2024]. Available at: https://journals.sagepub.com/doi/10.1038/jcbfm.2014.116.

[48] B. Lemasson, S. Valable, R. Farion, A. Krainik, C. Rémy, E.L. Barbier, In vivo imaging of vessel diameter, size, and density: A comparative study between MRI and histology: Vessel diameter, size, and density: MRI vs. Histology, Magn Reson Med [Internet] 69 (2013) 18–26 [cited 21 March 2023]. Available at: https://onlinelibrary.wiley.com/doi/10.1002/mrm.24218.

[49] C. Brossard, O. Montigon, F. Boux, A. Delphin, T. Christen, E.L. Barbier, et al., MP3: medical software for processing multi-parametric images pipelines, Front Neuroinform [Internet]. 14 (2020) [cited 21 October 2022]. 594799. Available at: https://www.frontiersin.org/articles/10.3389/fninf.2020.594799/full.

[50] T. Liu, C. Wisnieff, M. Lou, W. Chen, P. Spincemaille, Y. Wang, Nonlinear formulation of the magnetic field to source relationship for robust quantitative susceptibility mapping, Mag. Resonance Med [Internet] 69 (2013) 467–476 [cited 4 September 2024]. Available at: https://onlinelibrary.wiley.com/doi/10.1002/mrm.24272.

[51] Y. Wang, T. Liu, Quantitative susceptibility mapping (QSM): Decoding MRI data for a tissue magnetic biomarker, Mag. Resonance Med [Internet] 73 (2015) 82–101 [cited 4 September 2024]. Available at: https://onlinelibrary.wiley.com/doi/10.1002/mrm.25358.

[52] QSM Consensus Organization Committee, B. Bilgic, M. Costagli, K. Chan, J. Duyn, C. Langkammer, et al., Recommended implementation of quantitative susceptibility mapping for clinical research in the brain: A consensus of the ISMRM electro-magnetic tissue properties study group, Mag. Resonance Med [Internet] 91 (2024) 1834–1862 [cited 3 September 2024]. Available at: https://onlinelibrary.wiley.com/doi/10.1002/mrm.30006.

[53] H. Wei, R. Dibb, Y. Zhou, Y. Sun, J. Xu, N. Wang, et al., Streaking artifact reduction for quantitative susceptibility mapping of sources with large dynamic range: Streaking Artifact Reduction for QSM, NMR Biomed [Internet] 28 (2015) 1294–1303 [cited 4 September 2024]. Available at: https://onlinelibrary.wiley.com/doi/10.1002/nbm.3383.

[54] H.-G. Shin, J. Lee, Y.H. Yun, S.H. Yoo, J. Jang, S.-H. Oh, et al., X-Separation: magnetic susceptibility source separation toward iron and myelin mapping in the brain, NeuroImage [Internet]. 240 (2021) 118371 [cited 4 September 2024]. Available at: https://linkinghub.elsevier.com/retrieve/pii/S1053811921006479.

[55] M. Pei, T.D. Nguyen, N.D. Thimmappa, C. Salustri, F. Dong, M.A. Cooper, et al., Algorithm for fast monoexponential fitting based on Auto-Regression on Linear Operations (ARLO) of data, Mag. Resonance Med [Internet] 73 (2015) 843–850 [cited 4 September 2024]. Available at: https://onlinelibrary.wiley.com/doi/10.1002/mrm.25137.

[56] N.A. Pannetier, C.S. Debacker, F. Mauconduit, T. Christen, E.L. Barbier, A Simulation Tool for Dynamic Contrast Enhanced MRI. Louie A, Ed, PLoS ONE [Internet] 8 (2013) [cited 16 September 2024]. e57636. Available at: https://dx.plos.org/10.1371/journal.pone.0057636.

[57] F. Boux, F. Forbes, J. Arbel, B. Lemasson, E.L. Barbier, Bayesian inverse regression for vascular magnetic resonance fingerprinting, IEEE Trans. Med. Imaging 40 (2021) 1827–1837.

[58] N. Chou, Jiarong Wu, J. Bai Bingren, Anqi Qiu, Kai-Hsiang Chuang, Robust automatic rodent brain extraction using 3-D Pulse-Coupled Neural Networks (PCNN), IEEE Trans Image Process [Internet] 20 (2011) 2554–2564 [cited 31 May 2022]. Available at: http://ieeexplore.ieee.org/document/5729822/.

[59] M. Jenkinson, P. Bannister, M. Brady, S. Smith, Improved optimization for the robust and accurate linear registration and motion correction of brain images, NeuroImage 17 (2002) 825–841.

[60] D.A. Barrière, R. Magalhães, A. Novais, P. Marques, E. Selingue, F. Geffroy, et al., The SIGMA rat brain templates and atlases for multimodal MRI data analysis and visualization, Nat Commun [Internet] 10 (2019) 5699 [cited 11 July 2023]. Available at: https://www.nature.com/articles/s41467-019-13575-7.

[61] C.R. Harris, K.J. Millman, S.J. Van Der Walt, R. Gommers, P. Virtanen, D. Cournapeau, et al., Array programming with NumPy, Nature [Internet] 585 (2020) 357–362 [cited 21 May 2025]. Available at: https://www.nature.com/articles/s41586-020-2649-2.

[62] P. Virtanen, R. Gommers, T.E. Oliphant, M. Haberland, T. Reddy, D. Cournapeau, et al., SciPy 1.0: fundamental algorithms for scientific computing in Python, Nat Meth, [Internet] 17 (2020) 261–272 [cited 21 May 2025]. Available at: https://www.nature.com/articles/s41592-019-0686-2.

[63] S. Van Der Walt, J.L. Schönberger, J. Nunez-Iglesias, F. Boulogne, J.D. Warner, N. Yager, et al., scikit-image: image processing in Python, PeerJ [Internet] 2 (2014) [cited 21 May 2025]. e453. Available at: https://peerj.com/articles/453.

[64] T.-W. Tu, L.C. Turtzo, R.A. Williams, J.D. Lescher, D.D. Dean, J.A. Frank, Imaging of Spontaneous Ventriculomegaly and Vascular Malformations in Wistar Rats: Implications for Preclinical Research, J Neuropathol Exp Neurol [Internet] 73 (2014) 1152–1165 [cited 6 March 2024]. Available at: https://academic.oup.com/jnen/article-lookup/doi/10.1097/NEN.0000000000000140.

[65] M. Beaumont, B. Lemasson, R. Farion, C. Segebarth, C. Rémy, E.L. Barbier, Characterization of Tumor Angiogenesis in Rat Brain Using Iron-Based Vessel Size Index MRI in Combination with Gadolinium-Based Dynamic Contrast-Enhanced MRI, J Cereb Blood Flow Metab [Internet] 29 (2009) 1714–1726 [cited 21 March 2023]. Available at: http://journals.sagepub.com/doi/10.1038/jcbfm.2009.86.

[66] H.-L. Liu, P.-Y. Chen, H.-W. Yang, J.-S. Wu, I.-C. Tseng, Y.-J. Ma, et al., In vivo MR quantification of superparamagnetic iron oxide nanoparticle leakage during low-frequency-ultrasound-induced blood-brain barrier opening in swine, J. Magn. Reson. Imaging 34 (2011) 1313–1324.

[67] B. Marty, B. Larrat, M. Van Landeghem, C. Robic, P. Robert, M. Port, et al., Dynamic study of blood–brain barrier closure after its disruption using ultrasound: A quantitative analysis, J Cereb Blood Flow Metab [Internet]. 32 (2012) 1948–1958 [cited 19 October 2021]. Available at: http://journals.sagepub.com/doi/10.1038/jcbfm.2012.100.

[68] C. Cheng, H. Wan, P. Cong, X. Huang, T. Wu, M. He, et al., Targeting neuroinflammation as a preventive and therapeutic approach for perioperative neurocognitive disorders, J Neuroinflammation [Internet]. (2022) 19 [cited 17 July 2025]. Available at: https://jneuroinflammation.biomedcentral.com/articles/10.1186/s12974-022-02656-y.

[69] M.A. O'Reilly, O. Hough, K. Hynynen, Blood-brain barrier closure time after controlled ultrasound-induced opening is independent of opening volume: Blood-brain barrier closure time after ultrasound-induced opening, J Ultrasound Med [Internet] 36 (2017) 475–483 [cited 10 March 2022]. Available at: http://doi.wiley.com/10.7863/ultra.16.02005.

[70] P.-C. Chu, W.-Y. Chai, S.-T. Tsai, C.-H. Kang, C.-K. Yeh, H.-L. Liu, Focused ultrasound-induced blood-brain barrier opening: association with mechanical index and cavitation index analyzed by dynamic contrast-enhanced magnetic-resonance imaging, Sci. Rep. 6 (2016) 33264.

[71] F. Marques, J.C. Sousa, M.A. Brito, J. Pahnke, C. Santos, M. Correia-Neves, et al., The choroid plexus in health and in disease: dialogues into and out of the brain, Neurobiol. Dis. [Internet] 107 (2017) 32–40 [cited 27 May 2025]. Available at: https://linkinghub.elsevier.com/retrieve/pii/S0969996116302030.

[72] H. Lee, Y. Guo, J.L. Ross, S. Schoen, F.L. Degertekin, C. Arvanitis, Spatially targeted brain cancer immunotherapy with closed-loop controlled focused ultrasound and immune checkpoint blockade, Sci Adv [Internet]. 8 (2022) [cited 24 April 2023]. eadd2288. Available at: https://www.science.org/doi/10.1126/sciadv.add2288.

[73] T. Kobus, N. Vykhodtseva, M. Pilatou, Y. Zhang, N. McDannold, Safety Validation of Repeated Blood–Brain Barrier Disruption Using Focused Ultrasound, Ultrasound Med Biol [Internet] 42 (2016) 481–492 [cited 4 April 2022]. Available at: https://linkinghub.elsevier.com/retrieve/pii/S0301562915006237.

[74] B. Hiles-Murison, A.P. Lavender, M.J. Hackett, J.J. Armstrong, M. Nesbit, S. Rawlings, et al., Blood–brain barrier disruption and ventricular enlargement are the earliest neuropathological changes in rats with repeated sub-concussive impacts over 2 weeks, Sci Rep [Internet]. 11 (2021) 9261 [cited 4 April 2022]. Available at: http://www.nature.com/articles/s41598-021-88854-9.

[75] B. Lemasson, T. Christen, X. Tizon, R. Farion, N. Fondraz, P. Provent, et al., Assessment of multiparametric MRI in a human glioma model to monitor cytotoxic and anti-angiogenic drug effects, NMR Biomed [Internet] 24 (2011) 473–482 [cited 21 September 2023]. Available at: https://www.ncbi.nlm.nih.gov/pmc/articles/PMC3351072/.

[76] H. Fu, J. Zhou, S. Li, Y. Zhang, Z. Chen, Y. Yang, et al., Isoflurane impairs olfaction by increasing neuronal activity in the olfactory bulb, Acta Physiolog, [Internet]. 239 (2023) [cited 27 May 2025]. e14009. Available at: https://onlinelibrary.wiley.com/doi/10.1111/apha.14009.

[77] N. Lunardi, C. Hucklenbruch, J.R. Latham, J. Scarpa, V. Jevtovic-Todorovic, Isoflurane impairs immature astroglia development in vitro: The role of actin cytoskeleton, J Neuropathol Exp Neurol [Internet] 70 (2011) 281–291 [cited 27 May 2025]. Available at: https://academic.oup.com/jnen/article-lookup/doi/10.1097/NEN.0b013e31821284e9.

[78] Y. Yang, T. Liu, J. Li, D. Yan, Y. Hu, P. Wu, et al., General anesthetic agents induce neurotoxicity through astrocytes, Neural Regen. Res. [Internet]. 19 (2024) 1299–1307 [cited 27 May 2025]. Available at: https://journals.lww.com/10.4103/1673-5374.385857.

[79] H.J. Choi, M. Han, H. Seo, C.Y. Park, E.-H. Lee, J. Park, The new insight into the inflammatory response following focused ultrasound-mediated blood–brain barrier disruption, Fluids Barriers CNS [Internet] 19 (2022) 103 [cited 25 February 2024]. Available at: https://fluidsbarrierscns.biomedcentral.com/articles/10.1186/s12987-022-00402-3.

[80] A. Bellucci, O. Bugiani, B. Ghetti, M.G. Spillantini, Presence of reactive microglia and neuroinflammatory mediators in a case of frontotemporal dementia with P301S mutation, Neurodegener. Dis. 8 (2011) 221–229.

[81] K. Schoknecht, M. Maechler, I. Wallach, J.P. Dreier, A. Liotta, N. Berndt, Isoflurane lowers the cerebral metabolic rate of oxygen and prevents hypoxia during cortical spreading depolarization in vitro: an integrative experimental and modeling study, J. Cereb. Blood Flow Metab. 44 (2024) 1000–1012.

[82] N. McDannold, Y. Zhang, N. Vykhodtseva, Blood-brain barrier disruption and vascular damage induced by ultrasound bursts combined with microbubbles can be influenced by choice of anesthesia protocol, Ultrasound Med Biol [Internet] 37 (2011) 1259–1270 [cited 21 May 2021]. Available at: https://linkinghub.elsevier.com/retrieve/pii/S030156291100216X.

[83] T.A. Arsiwala, K.E. Blethen, C.P. Wolford, G.L. Pecar, D.M. Panchal, B. N. Kielkowski, et al., Single exposure to low-intensity focused ultrasound causes biphasic opening of the blood-brain barrier through secondary mechanisms, Pharm. Int. 17 (2025) 75 [cited 14 January 2025]. Available at: https://www.mdpi.com/1999-4923/17/1/75.